Research Square

Preprints are preliminary reports that have not undergone peer review.
They should not be considered conclusive, used to inform clinical practice,
or referenced by the media as validated information.

Episodic atmospheric transport reshapes cross-administrative methane attribution from Shanxi coal basins to Beijing-Tianjin-Hebei

Jason Cohen

jasonbc@alum.mit.edu

China University of Mining and Technology https://orcid.org/0000-0002-9889-8175

Yanqiu Liu

China University of Mining and Technology https://orcid.org/0009-0009-2966-6379

Kai Qin

China University of Mining and Technology https://orcid.org/0000-0002-1280-6330

Wei Hu

China University of Mining and Technology

Ge Han

Wuhan University

Lu Shen

Department of Atmospheric and Oceanic Sciences, School of Physics, Peking University
https://orcid.org/0000-0003-2787-7016

Hengkang Wang

Shanxi Academy of Eco-Environmental Planning and Technology

Kushal Tibrewal

UNEP's International Methane Emissions Observatory

Robert Field

UNEP's International Methane Emissions Observatory https://orcid.org/0000-0003-0228-1419

Article

Keywords:

Posted Date: November 4th, 2026

DOI: https://doi.org/10.21203/rs.3.rs-11402117/v1

License: This work is licensed under a Creative Commons Attribution 4.0 International License.
Read Full License

Additional Declarations: There is **NO** Competing Interest.

Episodic atmospheric transport reshapes cross-administrative methane attribution from Shanxi coal basins to Beijing-Tianjin-Hebei

Yanqiu Liu[1], Jason Blake Cohen[1,2*], Kai Qin[1,2*], Wei Hu[1], Ge Han[3], Lu Shen[4], Hengkang Wang[5], Kushal Tibrewal[6], Robert A. Field[6]

[1] *School of Environment and Spatial Informatics, China University of Mining and Technology, Xuzhou, China.*
[2] *Shanxi Key Laboratory of Environmental Remote Sensing Application, China University of Mining and Technology, Xuzhou, China.*
[3] *Hubei Key Laboratory of Quantitative Remote Sensing of Land and Atmosphere, School of Remote Sensing and Information Engineering, Wuhan University, Wuhan, China.*
[4] *Department of Atmospheric and Oceanic Sciences, School of Physics, Peking University, Beijing, China.*
[5] *Shanxi Academy of Eco-Environmental Planning and Technology, Taiyuan, China.*
[6] *UNEP's International Methane Emissions Observatory, Paris, France.*

[*]**Correspondence to:** Jason Blake Cohen (jasonbc@alum.mit.edu, jasonbc@cumt.edu.cn) and Kai Qin (qinkai@cumt.edu.cn)

Abstract

Methane mitigation is planned within administrative boundaries, but atmospheric transport redistributes methane across jurisdictions. Here we show that the methane-column response to Shanxi coal-mine emissions over the Beijing-Tianjin-Hebei megacity region is episodically amplified, while a key terrain gate is persistently undersampled by TROPOMI. A 4.5-year TROPOMI record, supported by independent Xianghe TCCON observations, demonstrates that the associated atmospheric organization and receptor relationships recur significantly beyond the originally simulated summer, including after excluding the entire 2022 calendar year. Controlled WRF-GHG experiments show that observation-constrained refinement of the Shanxi inventory increases mean downwind methane column mass by 15.2×10^3 tons relative to EDGAR, equivalent to 5.1% of the monthly regional emission benchmark (EBE), and that this response is amplified 3.36-fold under strong southwesterly flow. Valid TROPOMI retrievals cover only 0.13% of the gate-grid days, versus 8.6% regionally, with matched methane-carbon monoxide diagnostics linking the deficit to terrain-dependent screening. These findings reframe cross-boundary methane attribution as an episode resolved source-gate-receptor problem, linking source representation, atmospheric state, and observational coverage. Effective verification therefore requires coordinated source, pathway and receptor observations across the coupled airshed.

Introduction

Methane (CH_4) mitigation is implemented within administrative boundaries, yet its atmospheric signature is shaped by emissions and circulation across them[1,2]. With atmospheric methane at record highs and rapid emission reductions central to limiting near-term warming[3,4], connecting mitigation commitments to verifiable atmospheric evidence has become an urgent scientific challenge[5]. For a downwind jurisdiction, a change in methane abundance can reflect local abatement, changing upwind emissions or a reorganization of transport[1]. This ambiguity becomes especially consequential where major source regions and densely populated plains are separated by mountains. The regional influence of an emission source then depends on how circulation connects it to receptors, while the ability to verify that influence depends on where and when those connections are observed.

Northern China gives this problem a striking physical form. Shanxi accounts for approximately 15% of global coal production[6], with intensive coal-mine methane (CMM) emissions concentrated in basins such as Changzhi and Jincheng[7]. To the east, the Taihang Mountains rise between the coal-bearing highlands and the Beijing-Tianjin-Hebei (BTH) megacity cluster, with Shandong extending the downwind industrial region farther across the North China Plain. This landscape lends itself to a "leaky bathtub" interpretation: basin confinement favors local accumulation, while mountain passes and over-crest flow permit ventilation towards the plain[8] (Fig. 1; Supplementary Note 1). The ancient passes cutting through the Taihang thus provide a compelling setting in which to examine how terrain-mediated exchange links a major coal-producing province to neighboring jurisdictions. How strongly that connection changes with atmospheric conditions remains poorly quantified, even as Beijing and Tianjin implement methane-control plans within this shared airshed[9-11].

Satellite inversions have substantially improved regional and national methane emission estimates[12-14], while bottom-up and observation-constrained inventories reveal the spatial heterogeneity and temporal evolution of coal-mine emissions[15-17]. Studies of carbon monoxide (CO) and black carbon (BC) likewise demonstrate the value of combining satellite columns, surface measurements and vertical transport information to characterize industrial emissions and their regional influence[18-20]. These advances provide a basis for examining how the spatial distribution of emissions translates into a downwind atmospheric response. At Xianghe, previous regional modelling shows that meteorology can substantially alter the energy-sector methane signal even when the prescribed emissions remain relatively stable[21]. In a terrain-confined airshed, the location of active sources relative to ventilation pathways adds a further spatial dependence. Resolving how source heterogeneity and circulation interact is therefore essential to interpreting the atmospheric expression of emission changes across jurisdictions.

The observing system introduces a second, closely connected challenge. Methane retrievals and the emission estimates derived from them depend on surface properties, atmospheric conditions and spatial sampling[1,22,23]. A long satellite record may resolve regional variability while providing little direct information along particular mountain pathways. If sparsely observed terrain sectors also organize source-to-receptor transport, their absence can leave important atmospheric connections weakly constrained. Regional coverage statistics alone would conceal this mismatch. Identifying where transport pathways intersect persistent sampling gaps could establish priorities for complementary measurements, giving atmospheric transport analysis a direct role in the design of methane monitoring, reporting and verification (MRV).

Here we investigate this connection between source representation, episodic transport and observability in the Shanxi-BTH system. We incorporate an observation-constrained, high-resolution

Shanxi coal-mine inventory[17] into WRF-GHG and quantify the BTH methane-column response to its substitution for the corresponding EDGAR emissions[24] across 1608 hourly outputs in July-September 2022. A Terrain-XCH_4 Coupling Index, empirical orthogonal function decomposition (EOF) and three-dimensional transport diagnostics characterize broad advection and terrain-sensitive outflow with different receptor footprints. Regional emission-reduction and heterogeneous source-perturbation experiments examine complementary aspects of the simulated response. Four and a half years of TROPOMI satellite observations and multiyear TCCON measurements at Xianghe test whether the atmospheric organization and receptor relationships recur beyond the simulated period. Co-located AERONET aerosol measurements and TCCON observations of XCO and XCO_2 columns place the methane signal within the broader multigas environment of this industrial airshed.

We show that favorable synoptic conditions amplify the BTH response to refined Shanxi source representation more than threefold, while the long observational records reveal recurrent regional organization and receptor associations outside the simulated year. A model-identified terrain gate along the northern transport pathway, however, is sampled by valid TROPOMI retrievals on only 0.13% of grid-days, compared with 8.6% across the wider region. Comparisons with CO from the same satellite link this gap to terrain-dependent methane screening. Pathway geography and model-derived spatial correlation scales support Zhoukoudian and Dezhou as candidate locations for complementary ground-based monitoring. These findings extend the “leaky bathtub” picture from pollutant accumulation and ventilation to the practical problem of observing methane transport across jurisdictions. The resulting source-gate-receptor framework places episodic atmospheric connectivity and the capacity to observe its pathways at the center of cross-jurisdiction methane verification (Fig. 2). It informs monitoring priorities relevant to China’s Ecological and Environmental Code[25] and the Global Methane Pledge. The framework offers a transferable approach to examining source-receptor connections where concentrated emissions, complex terrain and jurisdictional boundaries are spatially misaligned, with potential applications in the Indo-Gangetic Plain, continental Southeast Asia and southern Africa.

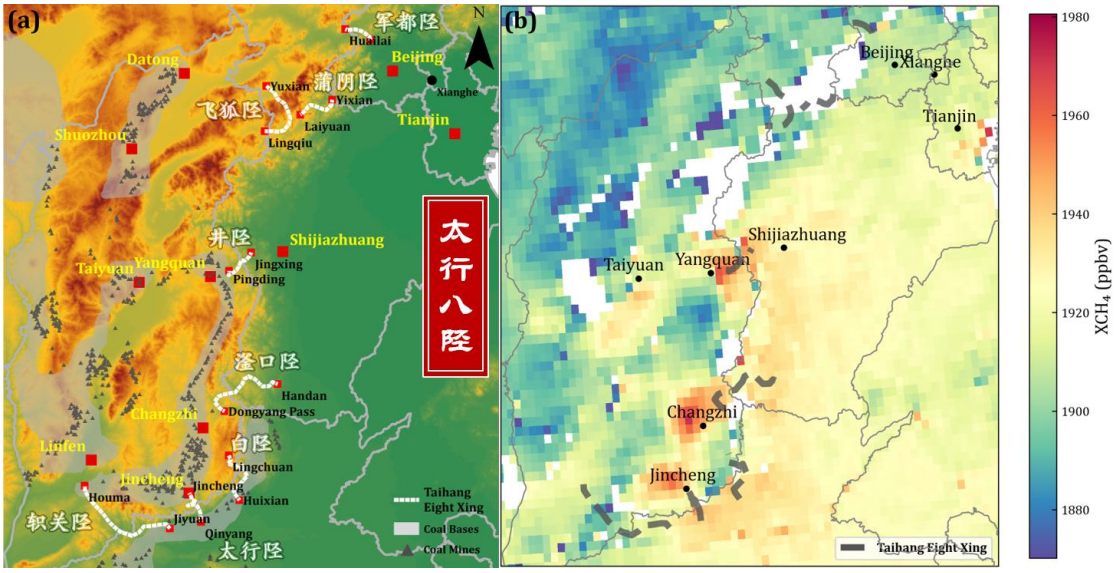

Fig. 1. Taihang Mountain passes and regional methane concentration distribution. (a) Geographic layout of the eight “Xing”, the ancient strategic mountain passes of the Taihang Mountains; (b) Satellite-derived methane spatial distribution across Shanxi and BTH (2022 annual-mean TROPOMI XCH_4).

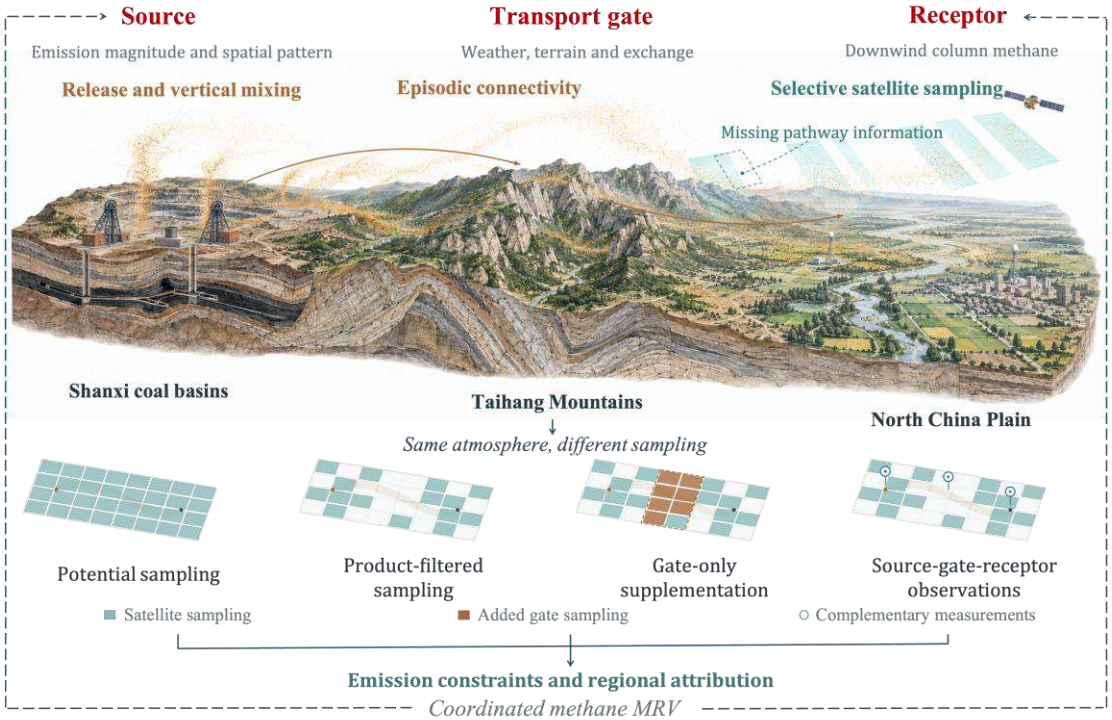

Fig. 2. Overview of the Source-Gate-Receptor Framework.

Results

Spatial fingerprint of coal mine methane and terrain-guided transport

High methane column concentrations (XCH_4 > 2.00 ppmv) in the SX-BTH domain coincide spatially with the coal-mine clusters of central Shanxi (Fig. 3a), consistent with the major role of these basins in regional methane emissions. Decomposition into background (BCK) and anthropogenic (ANT) components isolates the source-related pattern. BCK XCH_4 is comparatively uniform at approximately 1.91 ppmv (Fig. 3b), whereas ANT XCH_4 exceeds 80.0 ppbv over the mines and declines eastward across the Taihang Mountains towards the BTH Plain (Fig. 3c). The sharp transition across the mountains is consistent with terrain modulation of the cross-boundary methane gradient and provides the spatial context for the transport diagnostics below.

The Terrain-XCH_4 Coupling Index (Fig. 3d) identifies the topographic setting in which this gradient is expressed. A contiguous high-value channel extends from the high-elevation Shanxi plateau through the mountain passes into the low-elevation BTH Plain. It delineates a "source-terrain-receptor" configuration in which emissions released over the plateau encounter the northeast-southwest strike of the Taihang Mountains and the prevailing southwesterly circulation before reaching the BTH receptor region. The index therefore identifies the terrain-gated corridor that is subsequently reproduced by the EOF and three-dimensional transport diagnostics.

At the receptor Xianghe, EDGAR and Top-down show identical correlations with observed temporal variability (R = 0.46 for both; Fig. 3e). The Top-down simulation meets the criterion at 8 of the 10 high-column timestamps, compared with 6 of 10 for EDGAR. Error distributions provide a complementary diagnostic: the mean bias is +12 ppbv for EDGAR and +21 ppbv for Top-down (Fig. 3f). Thus, the refined Shanxi source field more frequently reaches the selected high-column amplitudes, whereas EDGAR yields the smaller mean offset. These diagnostics evaluate distinct aspects of model performance and do not by themselves identify a unique source of the receptor mismatch. Together, the

spatial fields and Xianghe comparisons provide the source-receptor context for the pathway and paired-response analyses below.

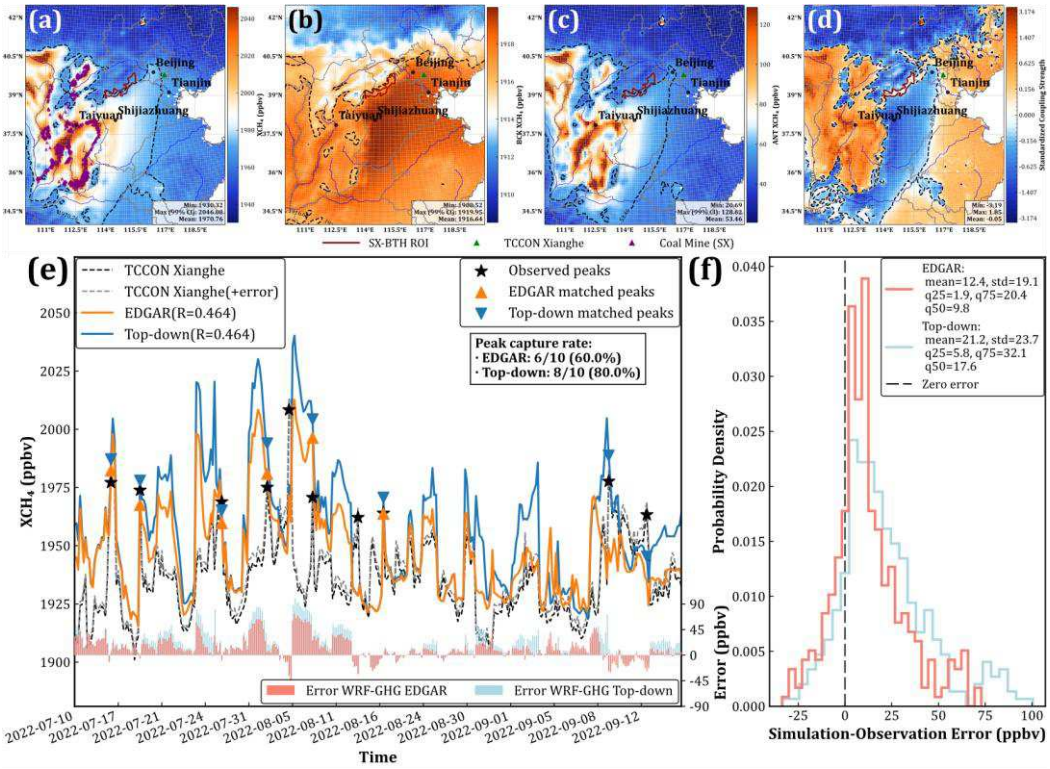

Fig. 3. Simulated methane components, terrain coupling and Xianghe receptor evaluation over the SX-BTH domain. (a-c) Total, BCK and ANT XCH_4 from the merged inventory; (d) Terrain-XCH_4 Coupling Index; (e) hourly XCH_4 at TCCON Xianghe, with selected high-column timestamps and simulations meeting the one-sided magnitude criterion indicated; (f) simulation-observation error distributions at matched TCCON retrieval hours.

Complementary transport configurations revealed by EOF decomposition

EOF decomposition of the area-weighted, detrended XCH_4 field over the SX-BTH domain (d02, 9 km resolution) identifies three leading modes accounting for 48% of regional variance (Fig. 4). EOF1 explains 25% and describes broad regional variability across much of the domain. EOF2 explains 14% and exhibits a coherent meridional dipole, while EOF3 explains 8.7% and captures a more localized, heterogeneous pattern. These spatial differences provide a basis for examining how the Shanxi source region connects to different parts of the downwind plain.

The long record TROPOMI decomposition provides an independent test of the model's spatial structure. Across 4618 common grid cells, the centered, area-weighted correlation between model EOF2 and TROPOMI EOF2 is 0.90 (95% spatial-block CI: [0.85, 0.93]). The TROPOMI pattern also provides an external anchor within the model EOF2-EOF3 subspace, requiring a rotation of only 4.2° to align the model basis with the satellite EOF2 direction (Figs. S17-S19 and Table S7), while also preserving the model's complementary EOF3 residual direction. Over the common 1608-h ΔM_{inv} window, including PC2 in the nested regression with 24-lag HAC covariance leaves the conditional PC1 and PC3 point estimates almost unchanged, with shifts of -0.53% and +0.52%, respectively (Table S9). This external anchoring demonstrates that the short WRF-GHG record reproduces the observed spatial organization of methane variability, and supports the interpretation of EOF1 and EOF3 as distinct transport configurations within a physically realistic model framework.

EOF1 and EOF3 describe distinct source-receptor geometries across the Taihang Mountains. The broad EOF1 pattern is consistent with southwesterly advection from the Shanxi plateau towards the BTH

Plain. Its high-value contours cluster near Beijing and weaken towards Shijiazhuang, Tianjin and Tangshan, delineating its northern Taihang expression (Fig. 4a). EOF3 is associated with the Changzhi-Jincheng source region, with positive loadings extending across southern Hebei into Shandong, where the mode reaches its maximum (Fig. 4c). Within the SX-BTH framework examined here, Beijing lies within the principal northern footprint of EOF1 and near the northern margin of the southern EOF3 configuration. This difference in receptor position motivates separate examination of the two pathways and their vertical transport structures. The pronounced EOF3 extension into Shandong places the BTH response within a wider North China airshed and calls for complementary observations along the northern Taihang-Beijing corridor and the southern Hebei-Shandong extension. The subsequent BTH mass-response analysis uses PC1 and PC3 to classify these transport conditions and evaluates the full paired-simulation mass response within each class.

PC1 and PC3 also differ in their temporal evolution. PC1 varies on a broader synoptic timescale, whereas PC3 exhibits more rapid fluctuations associated with intermittent terrain-sensitive export (Fig. 4d). In the autocorrelated 2022 model record, the PC1-PC3 cross-correlation reaches a descriptive maximum at a positive lag of 28 h ($r = 0.47$), consistent with synoptic buildup preceding terrain-sensitive enhancement. Individual high-column episodes display considerable variation around this ordering. Normalized PC trajectories within the selected event windows show both synchronous PC1-PC3 amplification and events dominated by either configuration (Fig. 4e), indicating that receptor extremes develop under different combinations of regional and terrain-sensitive variability. The following transect analyses examine the wind fields and vertical methane structure associated with these contrasting spatial configurations and event sequences (Figs. 5 and 6).

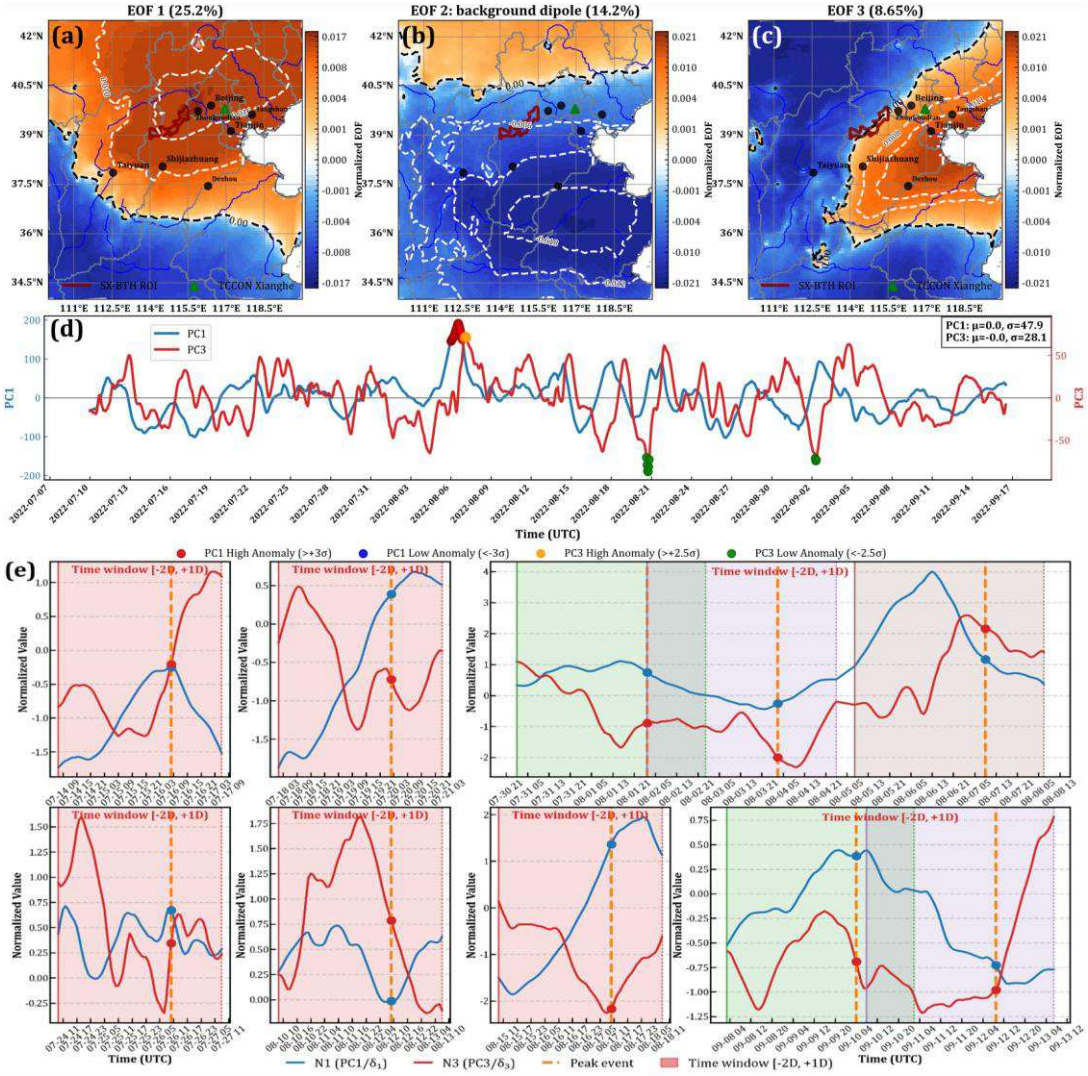

Fig. 4. EOF and PC analysis of XCH_4 spatiotemporal variability over the SX-BTH domain. (a) EOF1 spatial pattern (25.2% explained variance), representing the broad synoptic configuration; positive contours delineate its northern Taihang expression. (b) EOF2 spatial pattern (14.2%), showing a meridional dipole retained in the regional decomposition. (c) EOF3 spatial pattern (8.7%), representing a localized terrain-sensitive configuration associated with the Changzhi-Jincheng source region; positive loadings extend across southern Hebei towards Shandong. (d) PC1 and PC3 time series showing the temporal evolution of the two configurations. (e) Normalized PC1 (N1) and PC3 (N3) time series within high-column windows spanning -2 to +1 d, illustrating both synchronous and asynchronous mode activation.

Two complementary transport pathways diagnosed from EOF modes

Transect analyses reveal how the broad EOF1 and more localized EOF3 configurations are expressed in the along-path evolution and vertical column structure of methane across the Taihang Mountains.

Path 1: Synoptic-scale advection (EOF1). The northern transect extends from northeastern Shanxi towards the Beijing-Xianghe sector (Fig. 5a). During PC1 anomalies, total XCH_4 shows a coherent enhancement along the transect (Fig. 5c-d). The anthropogenic component exhibits a distinct enhancement band that progresses downstream towards the receptor region (Fig. 5f), providing a direct view of the along-path evolution underlying the total-column increase. This coherent progression is consistent with regional advection of anthropogenic tracers[20,26,27]. The accompanying wind distribution

changes markedly with height (Fig. 5b). Height-resolved column diagnostics show that the event enhancement persists when near-surface layers are excluded from the integration, indicating that the signal extends beyond the lowest layers (Fig. 5g-j). The lower segment of the partial-column profile has a slope of approximately -46 ppbv km^{-1}, reflecting the pronounced contribution of methane-rich lower layers to the column signal.

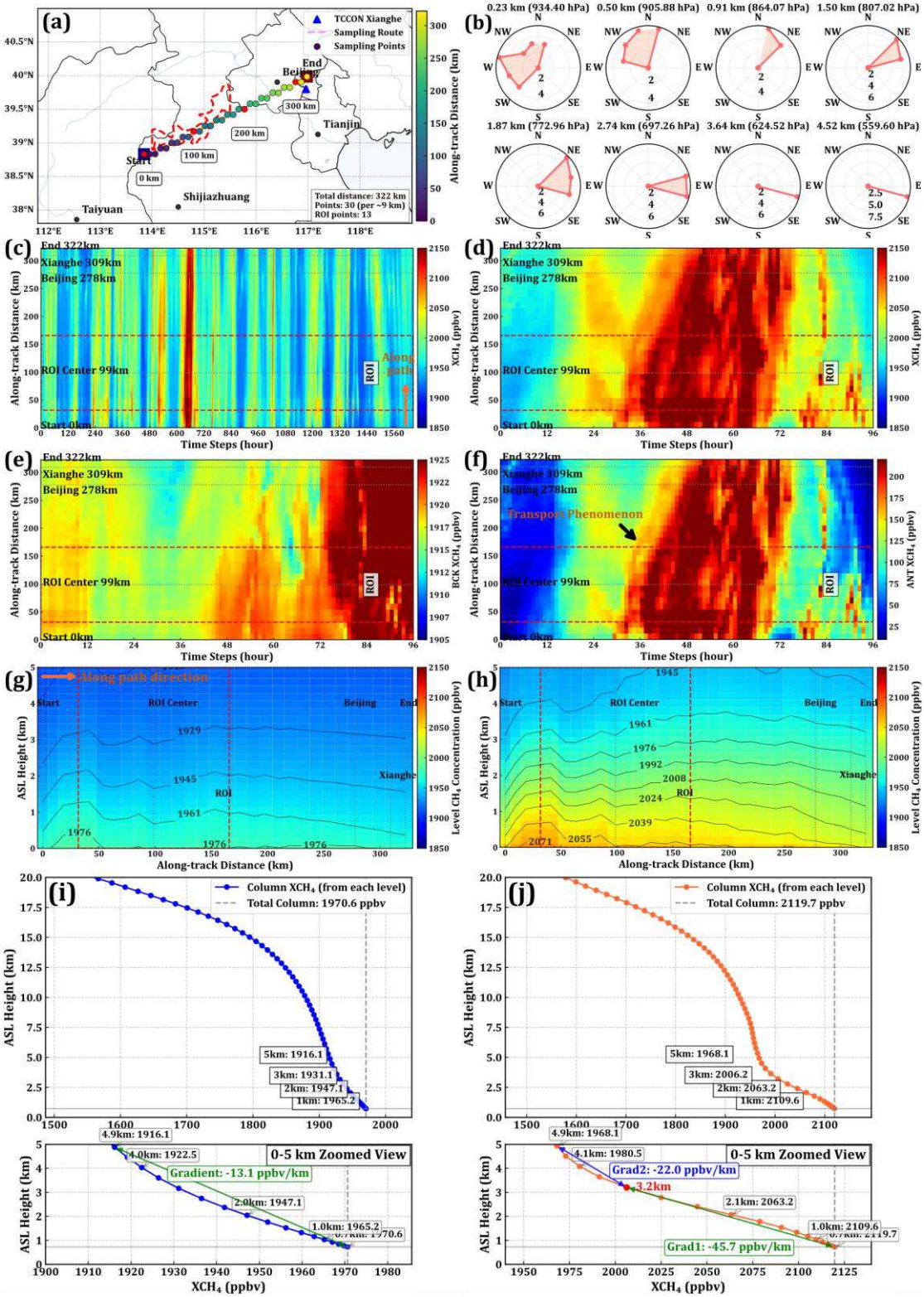

Fig. 5. EOF1-associated methane transport diagnostics. (a) Path 1 diagnostic sampling transect; (b) Wind roses from WRF simulations (0.230-4.52 km a.g.l., PC1 anomaly period); (c-d) Time-distance distributions of total XCH_4

over the full simulation record and PC1 anomalies; (e-f) BCK and ANT XCH_4 (PC1 anomalies); (g-h) Vertical partial-column XCH_4 profiles (full period and PC1 anomalies); (i-j) Partial-column gradients (full period and PC1 anomalies) in the ROI. Partial-column XCH_4 denotes the column-averaged mole fraction integrated from each indicated starting height to the model top.

Path 2: Terrain-sensitive emission flushing (EOF3). The southern transect begins near the Changzhi coal basin and extends northeastward across Hebei towards the BTH receptor region (Fig. 6a). During PC3 anomalies, ANT enhancements develop as several distinct pulses, producing an intermittent and spatially uneven progression along the transect (Fig. 6c-d). The wind distribution also varies substantially with height during the sampled event days (Fig. 6b). The strongest column enhancements are concentrated over the upstream and intermediate portions of the transect (Fig. 6e-f). As methane-rich lower layers are excluded from the integration, the partial-column profile declines sharply, with a lower-segment slope of approximately -48 ppbv km^{-1} (Fig. 6g-h). These features characterize the localized expression of the southern export configuration.

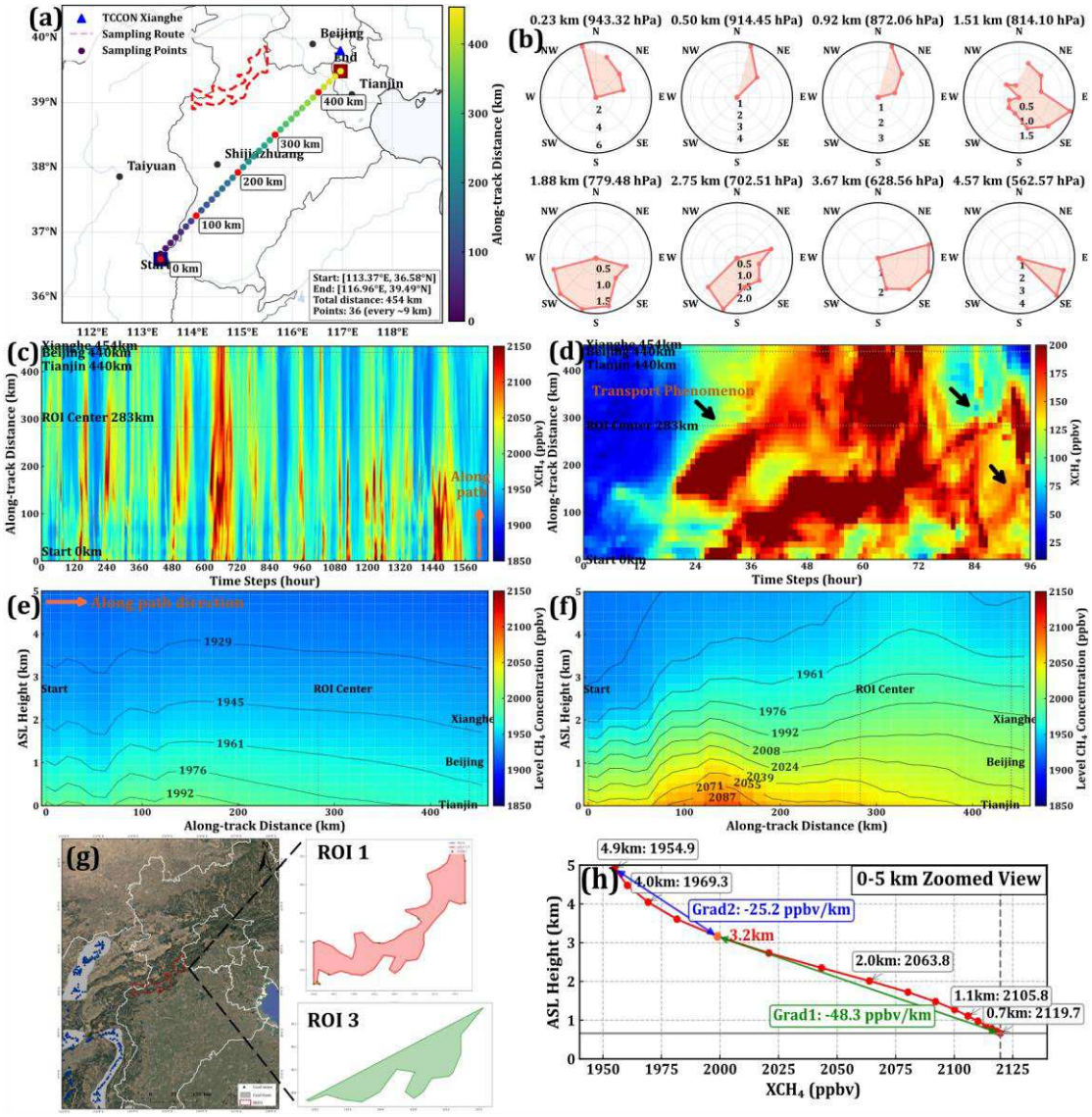

Fig. 6. Diagnostics of EOF3-associated methane transport. (a) Path 2 diagnostic sampling transect; (b) Wind roses (0.230-4.57 km a.g.l., PC3 anomaly period); (c) Time-distance distribution of total XCH_4 over the full simulation record; (d) Time distance distribution of ANT XCH_4 during PC3 anomalies; (e-f) Vertical partial-

column XCH_4 profiles (full period and PC3 anomaly period); (g) ROI3 schematic (lower ROI segment within EOF3 high-value boundary); (h) Partial-column gradients over ROI3 (PC3 anomaly period).

The contrast between coherent northern advection and intermittent southern export provides the physical context for evaluating episode-scale receptor enhancements and the atmospheric dependence of the BTH mass response. Their different receptor footprints also motivate the subsequent long-record analyses of recurrence and observational coverage across the wider airshed.

Targeted source perturbations and receptor observations constrain high-column amplitudes

To test how spatial heterogeneity in Shanxi's coal-mine methane inventory affects downwind BTH concentrations, we performed targeted emission perturbation experiments. The perturbations are applied only to Shanxi's coal-mining grids (Fig. 7a), while the model resolves their atmospheric response throughout the downwind domain; emissions outside those source grid cells remain unchanged. The ±50% perturbation is deliberately wider than the estimated 10-30% coherent regional source-scale sensitivity (Supplementary Notes 2 and 5; Figs. S3 and S8), providing a stringent test of how source heterogeneity propagates into receptor extremes.

The ±50% perturbation retains a temporal association with TCCON comparable to Top-down (R = 0.483 and 0.464, respectively; Fig. 7b). In the fixed valid-record hourly cohort, Top-down and EDGAR meet the one-sided magnitude criterion at 8 of 10 and 6 of 10 selected high-column timestamps, respectively. In the separately defined nominal 30-min cohort, the ±50% perturbation and BTH-50% simulations meet the same criterion at 9 of 10 and 4 of 10 timestamps, respectively (Fig. 7c; Tables S2 and S3). Reducing BTH anthropogenic emissions by 50% lowers the Xianghe mean bias from +21 to +6.1 ppbv and the RMSE from 32 to 20 ppbv, while the correlation decreases to R = 0.42. Mean-state agreement and high-column magnitude capture therefore constrain different aspects of receptor performance.

Under the ±50% perturbation, the sole selected high-column timestamp outside the magnitude criterion occurs on 4 August 2022 at 02:00 UTC (TCCON XCH_4 = 2008 ppbv), with a coincident high AOD_{440} of 2.28, so its observed amplitude is treated as potentially aerosol-sensitive. High aerosol loading was recurrent, with at least one $AOD_{440} > 0.8$ retrieval on 363 of 1093 observed days in the entire data record (Fig. S24). Across 678 overpass-window days in the multi-year Xianghe record, XCH_4 covaries with AOD_{440} at +28 ppb AOD_{440}^{-1} (95% 28-calendar-day block-bootstrap CI: [24, 33]). On the 533 days common to XCH_4, XCO, XCO_2 and AOD_{440}, the corresponding gas-normalized associations are +1.7 for XCH_4 (95% CI: [1.4, 2.0]), +1.94 for XCO ([1.6, 2.3]) and +1.4 for XCO_2 ([1.0, 1.8]), all in gas-anomaly SD AOD_{440}^{-1} (Fig. 7e). Native-unit slopes are reported in Fig. S21. The coherent positive associations of XCH_4, XCO and XCO_2 with AOD_{440} place the Xianghe methane record within an aerosol-rich, multispecies atmospheric context in which co-emitted species from industrial sources near the coal mine sources, atmospheric processing and regional transport can all contribute[18-20,28]. AOD leaves particle-size distribution, mixing state and wavelength-dependent absorption unresolved[19,29-31], while XCH_4, XCO and XCO_2 are retrieved from the same direct-sun spectra. Atmospheric covariance and residual retrieval sensitivity therefore remain partially inseparable. In the joint receptor model containing standardized AOD, PC1, PC2, PC3, season and year, the satellite-derived mode associations remain positive after exclusion of the complete 2022 calendar year: +5.1 ppb SD^{-1} for PC1 (95% CI: [4.0, 6.05]), +2.1 ppb SD^{-1} for PC2 ([0.92, 3.4]) and +1.9 ppb SD^{-1} for PC3 ([1.2, 2.8]; n = 430; Fig. S22). Event-level aerosol sensitivity of the selected high-column cohort is reported in Fig. S23, while the 4 August timestamp and its coincident AOD are documented in Tables S2-S3.

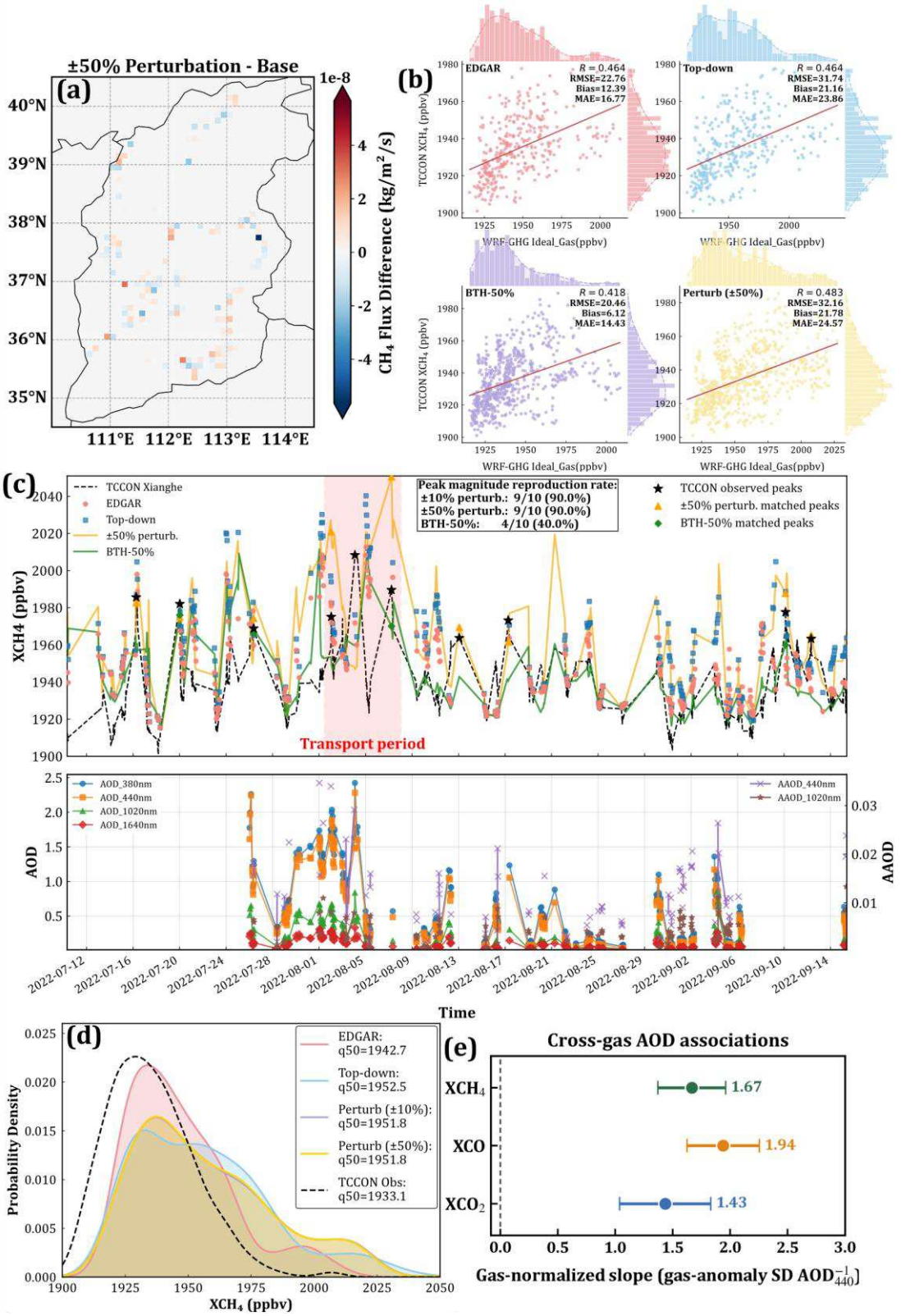

Fig. 7. Xianghe receptor evaluation across source-field, regional-emission and aerosol conditions. (a) Spatial distribution of CH_4 flux differences for the ±50% Shanxi source-field perturbation relative to Top-down during August 2022. Perturbations are restricted to coal-mining source grids, while their atmospheric response extends downwind. (b) Statistical validation of WRF-GHG XCH_4 simulations against TCCON Xianghe observations. (c) Nominal 30-min time series of simulated XCH_4 and TCCON observations, together with concurrent aerosol optical

depth. Black stars mark the ten high-column timestamps selected from the nominal 30-min valid-record sequence; symbols identify timestamps at which the ±50% perturbation and BTH-50% simulations meet the one-sided magnitude criterion. The annotation reports the corresponding nominal-cohort counts for Perturb±10%, Perturb±50% and BTH-50%. The separately selected hourly EDGAR-Top-down cohort is reported in Table S2. (d) Probability density functions of simulated and observed XCH_4. (e) Gas-normalized associations of deseasonalized Xianghe XCH_4, XCO and XCO_2 with co-located AERONET AOD_{440} over 533 common days. Slopes are normalized by the standard deviation of each trace-gas anomaly, while AOD_{440} remains on its native scale. Points and error bars denote estimates and 95% seven-lag Newey-West intervals.

Episodic quantification of cross-administrative methane-column responses

To quantify paired methane-column responses to the refined Shanxi CMM inventory, specified regional emission reductions and Shanxi source-field perturbations, we derived column-mass response metrics (ΔM, units: tons) from five simulation configurations (see Methods for experimental details).

Regional mass response. During August 2022, the observation-constrained refinement of the Shanxi coal-mine inventory (Δ_{inv}) produces a mean BTH column-mass response of 15.0×10^3 tons, equivalent to 5.01% of the monthly EDGAR baseline emission (EBE = 298,956 tons; Table 1A), with hourly values reaching 53.7×10^3 tons. Across the full 1608-h analysis, Δ_{inv} averages 15.2×10^3 tons. During the 21 h with PC1 > +3σ, when sustained southwesterly flow connects the Shanxi Plateau with the North China Plain, the conditional mean reaches 51.2×10^3 tons, equivalent to 17.1% of EBE and a 3.36-fold amplification relative to the full-period mean (Table 1B). During the four hours when both PC1 and PC3 > +2σ, the response reaches 42.7×10^3 tons, equivalent to 14.3% of EBE and a 2.80-fold amplification. This episodic contrast is spatially consistent with the southeastern Shanxi and southern Hebei sector identified by the EOF and three-dimensional diagnostics. The inventory-refinement composites show a broad synoptic enhancement under PC1 > +3σ and a more localized terrain-sensitive response under PC3 > +2σ (Fig. 8c-d). These results show that atmospheric organization strongly modulates the magnitude of the cross-administrative methane-column response.

Source-field sensitivity. The deliberately broad, ±50% spatial perturbation (Δ_{SX}) produces an August-mean response of 60.7 tons, equivalent to 0.0203% of EBE, while individual hourly responses reach 24.4×10^3 tons (Table 1A). The small period mean reflects compensation among positive and negative responses to the spatially heterogeneous perturbation, whereas the hourly excursions demonstrate substantial event-scale sensitivity when regional transport pathways are active. This result complements the receptor evaluation by showing that source-field heterogeneity can alter individual event amplitudes without imposing a comparable shift in the August mean.

Regional scenario contrasts of the BTH response. The BTH-50% and BJ-50% experiments reveal a pronounced spatial asymmetry in the signed response to receptor-region emission reductions (Table 1A). Halving anthropogenic emissions across BTH produces a mean BTH column-mass response of 29.5×10^3 tons, whereas the corresponding Beijing-only response is negligible in magnitude at -93.5 tons. The algebraic Tianjin-Hebei residual, Δ_{TH}, is therefore 29.6×10^3 tons, equivalent to 9.90% of the monthly EBE. Across all 326 TCCON timestamps within the 1608-h analysis window, the native-grid signed Beijing scenario contrast remains centered close to zero, with a median of +0.577 ppbv. During the ten selected high-column timestamps, the Tianjin-Hebei residual intensifies to a median of +29.4 ppbv, with a mean of +25.2 ppbv and a maximum of +70.2 ppbv (Fig. S16 and Table S6).

Together, these experiments separate the modest period-mean response from its synoptic amplification and show that receptor-region emissions and upwind source representation govern different aspects of the Xianghe signal.

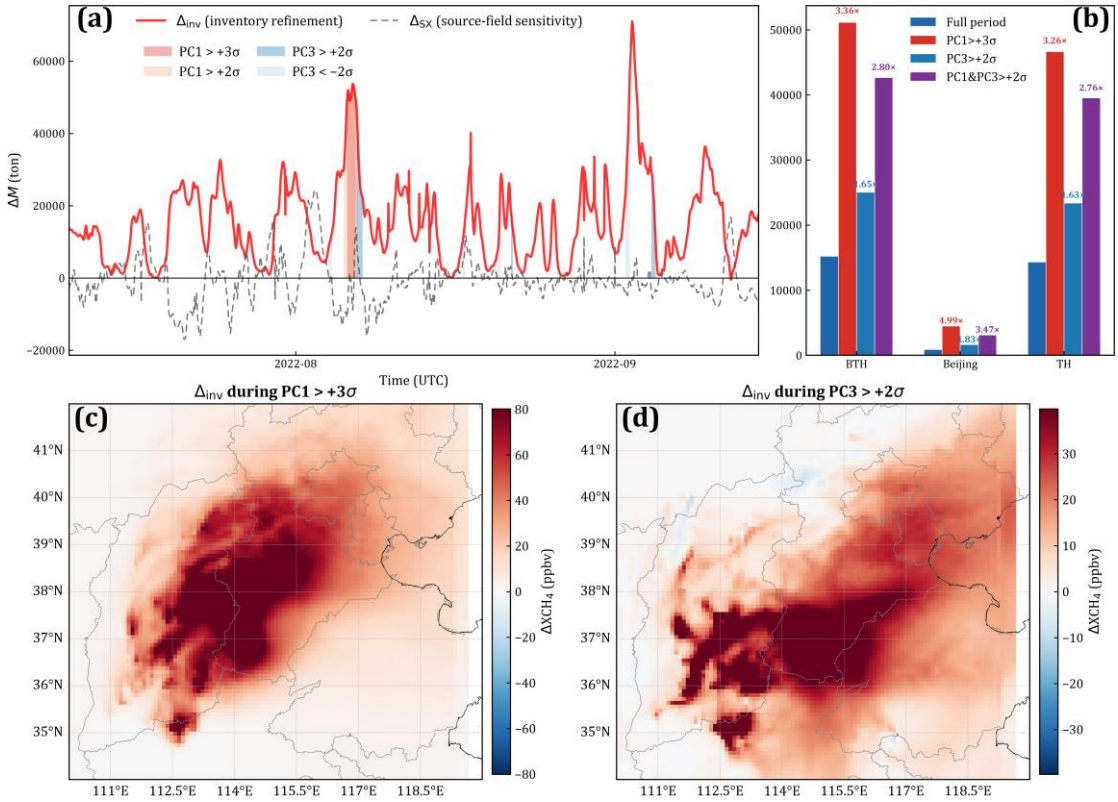

Fig. 8. Episodic amplification of the BTH methane-column response to the refined Shanxi coal-mine inventory. (a) Time series of column-integrated mass response Δ_{inv} (inventory refinement) and Δ_{SX} (source-field sensitivity) over the BTH domain. Shaded intervals highlight periods exceeding the indicated PC1/PC3 thresholds. (b) Mean Δ_{inv} during the full period and under key synoptic regimes, integrated over the BTH region, Beijing municipality, and the Tianjin-Hebei (TH) subregion. Amplification factors are annotated. (c-d) Spatial distributions of mean Δ_{inv} during PC1 > +3σ and PC3 > +2σ periods, respectively. Concentration units (ppbv) emphasize transport gradients independent of grid-cell area.

Table 1. BTH CH_4 column-mass responses and synoptic amplification.

A. Scenario contrasts during August 2022.

Attribution metric	Region	Mean ΔM (ton)	Maximum ΔM (ton)	% of EBE
	BTH	15.0×10^3	53.7×10^3	5.01
Δ_{inv}	Beijing	935	5.77×10^3	3.23
	Xianghe	5.07	31.5	2.07
Δ_{SX}	BTH	60.7	24.4×10^3	0.0203
Δ_{BTH}	BTH	29.5×10^3	111×10^3	9.87
Δ_{BJ}	BTH	-93.5	16.2×10^3	-0.0313
Δ_{TH}	BTH	29.6×10^3	113×10^3	9.90

B. EOF-stratified amplification of Δ_{inv} over the BTH region.

Condition	N (hours)	Mean ΔM (ton)	% of EBE	Amplification
Full period	1608	15.2×10^3	5.09	1.00×
PC1 > +3.0σ	21	51.2×10^3	17.1	3.36×
PC1 > +2.0σ	34	46.9×10^3	15.7	3.08×
PC3 > +2.0σ	31	25.0×10^3	8.38	1.65×
PC1 and PC3 > +2.0σ	4	42.7×10^3	14.3	2.80×

PC1 < -2.0σ	20	2.44×10^3	0.817	0.160×

EBE is a descriptive normalization benchmark defined as one month of EDGAR anthropogenic CH_4 emissions integrated over the native WRF mass grid for the geographic unit specified in each row. EBE-normalized percentages express the simulated column-mass response relative to this benchmark and do not represent source fractions or transport efficiencies. Δ_{BTH} and Δ_{BJ} are signed responses to the corresponding 50% emission reductions, and Δ_{TH} is their algebraic Tianjin-Hebei residual. Section A Δ_{SX} statistics use common HH:00 UTC pairs. Section B statistics are calculated from 00:00 UTC on 10 July through 00:00 UTC on 15 September 2022. The concurrent PC1-PC3 condition contains four hours and should be interpreted cautiously.

Long-record observations resolve atmospheric organization and receptor expression

Atmospheric mechanisms that govern cross-boundary methane-column responses should leave an imprint beyond a single simulated summer. We therefore examined four and a half years of daily TROPOMI XCH_4 on the common analysis grid together with independent column observations at Xianghe. At the pre-specified +1-day lag, the exact-calendar PC1-PC3 association is r = 0.20 (95% 14-calendar-day block-bootstrap CI: [0.136, 0.262]; n = 1486; Fig. 9a), indicating approximately 4% of days are impacted by this dual-driven flow. The association remains positive after excluding the complete 2022 calendar year (r = 0.208, 95% CI: [0.135, 0.273]; n = 1161) and in post-2022 observations (r = 0.178, 95% CI: [0.106, 0.253]; n = 988). The persistence of this relationship beyond 2022 supports recurring temporal organization within the satellite record.

The receptor record resolves how the three leading modes are expressed at Xianghe. Across 696 exact-date TROPOMI-PC-TCCON matches, the common PC > +1 full-record SD (σ) criterion yields event-minus-non-event XCH_4 differences of +16 ppb for PC1 (95% CI: [11.6, 20.3]), +1.33 ppb for PC2 (95% CI: [-3.18, 5.83]) and +4.44 ppb for PC3 (95% CI: [0.697, 8.53]; Fig. 9b). In the joint model containing PC1, PC2, PC3, season and year, the corresponding full-record conditional coefficients are +8.40 ppb SD^{-1} for PC1 (95% 28-calendar-day block-bootstrap CI: [7.08, 9.76]), +1.81 ppb SD^{-1} for PC2 (95% CI: [0.578, 3.17]) and +3.1 ppb SD^{-1} for PC3 (95% CI: [2.01, 4.16]; Fig. 9c). The PC1 and PC3 associations remain positive after exclusion of the complete 2022 calendar year, with coefficients of +7.92 ppb SD^{-1} (95% CI: [6.45, 9.31]) and +3.41 ppb SD^{-1} (95% CI: [2.29, 4.75]), respectively (n = 491). The corresponding post-2022 coefficients are +8.32 ppb SD^{-1} (95% CI: [7.03, 9.72]) and +3.61 ppb SD^{-1} (95% CI: [2.25, 5.03]), respectively (n = 378). These cohorts provide a receptor-side out-of-window test that is independent of the simulated episode. Projection of the long-record anomalies onto the WRF-GHG EOF patterns provides a complementary transfer test: after exclusion of 2022, PC1 and PC3 retain positive conditional Xianghe associations of +12.8 and +3.79 ppb SD^{-1}, respectively (Table S10). PC1 provides the largest receptor association, PC3 retains a distinct positive association across both out-of-window cohorts. In the satellite-native decomposition, PC2 is positive in the continuous joint model although its threshold-event contrast spans zero.

Together, these observations support recurrence of the model-defined spatial organization and its receptor expression. Broad synoptic variability provides the largest Xianghe signal, while the terrain-sensitive configuration retains distinct information at the receptor. The remaining question is whether the satellite record adequately observes the terrain gate through which this organization is expressed.

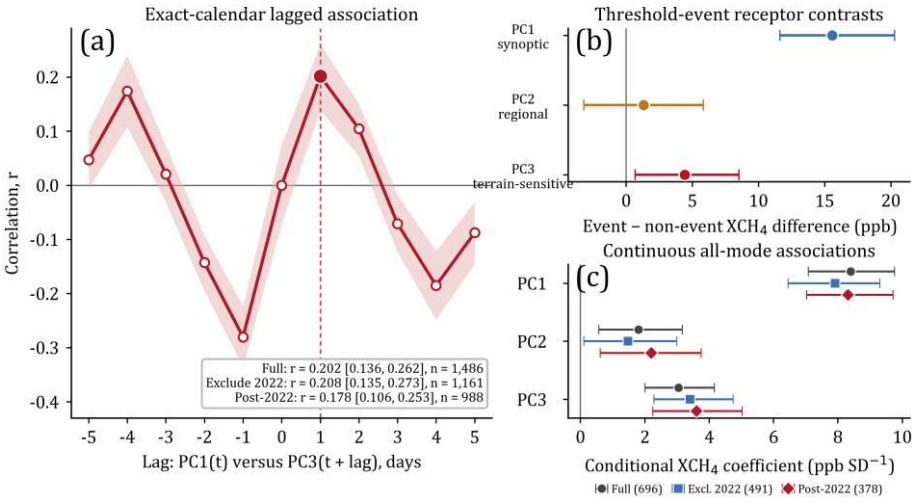

Fig. 9. Long-record lagged association and joint three-mode receptor signatures. (a) Exact-calendar correlations between TROPOMI PC1(t) and PC3(t + lag) over the 4.5-year record. Positive lags indicate that PC1 leads PC3. Shading denotes 95% intervals from a 14-calendar-day circular moving-block bootstrap; the annotation reports the +1-day estimates for the full record, after exclusion of 2022 and for post-2022 observations. (b) Event-minus-non-event Xianghe XCH_4 differences for PC1, PC2 and PC3 across 696 exact-date TROPOMI-PC-TCCON matches, using PC > +1 full-record SD for each mode. Error bars denote 95% 14-calendar-day block-bootstrap intervals. (c) Partial regression coefficients from the joint PC1-PC2-PC3, season and year model for the full record, the 2022-excluded cohort and post-2022 observations. Error bars denote 95% intervals from a 28-calendar-day circular moving-block bootstrap. Leave-one-year-out results are reported in Table S8.

The terrain gate is selectively under-observed in satellite record

The extended satellite record reveals an observational limitation that is directly relevant to cross-boundary attribution. We delineated the terrain gate from the model-derived PC1 Terrain-XCH_4 field independently of satellite retrieval availability, and then evaluated its representation in the final-QC TROPOMI record. Only 0.126% of gate grid-days contain a valid retrieval, compared with 8.56% across the SX-BTH analysis domain (Fig. 10a), leading to a gate sampling rate approximately 68-fold lower than the domain. The deficit persists across the 4.5-year record and is not confined to a small number of adverse months (Fig. 10b).

The deficit persists after balancing mean latitude, longitude and elevation and is evident in every season (Fig. S20; Supplementary Note 7). Observations of CO from the same satellite reveal a marked contrast along this pathway. On 1264 orbit-paired dates during July 2021-December 2024, the gate-to-weighted-comparison coverage ratio was 1.13 for clear-sky/clear-sky-like CO, compared with 0.00797 for CH_4 (Fig. 10c). CO coverage remains incomplete, leaving most gate grid-days unobserved. The spatially balanced comparison nevertheless identifies a pronounced gate-specific deficit in CH_4 that is absent in CO.

Native-pixel matching links this contrast to the methane screening process. Among scenes with valid clear-sky/clear-sky-like CO, the reported terrain-roughness filter constitutes 74.1% of the weighted CH_4 processing-status distribution over the gate, compared with 14.9% in the non-gate comparison (Fig. 10d). The gate also exhibits greater within-footprint elevation variability (Fig. S25c). These diagnostics show how the complex terrain that guides the modelled transport also restricts its representation in the satellite methane record.

This alignment of transport geography and retrieval loss gives a practical focus to complementary network design. The NMC analysis yields a 149 km horizontal forecast-error correlation length, which

is close to the 151 km XCH_4 signal scale derived separately from the same simulation (Supplementary Note 7; Fig. S15a). Along the Yangquan-Zhoukoudian-Xianghe transect, the fitted correlation declines from 0.838 over the 89 km Zhoukoudian-Xianghe segment to 0.157 across the 287 km Yangquan-Zhoukoudian separation. Zhoukoudian, within the high-loading expression of EOF1, is a natural intermediate candidate for resolving the northern Taihang configuration. Dezhou, within the EOF3 lobe, provides a complementary downstream candidate for observing terrain-sensitive export. The screening diagnostics also identify terrain-dependent pathway coverage as a consideration for future satellite mission design (Supplementary Note 8). The correlation scale supplies a physically based separation criterion for a complementary network spanning both transport configurations and their administrative receptors; formal network optimization would require additional constraints. This scale is two to three times larger than reported for CO[32], consistent with methane's weaker sensitivity to local chemical processing.

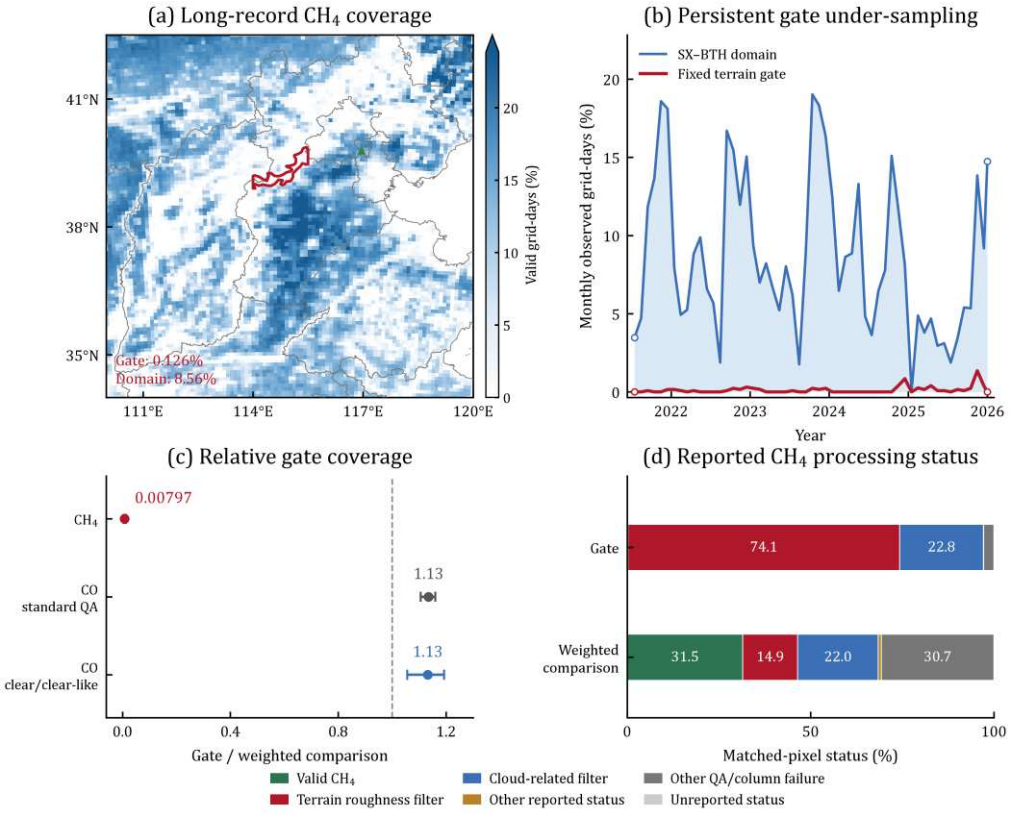

Fig. 10. Terrain-dependent methane under-observation along the model-defined transport gate. (a) Valid TROPOMI CH_4 grid-day coverage from July 2021 to December 2025. (b) Monthly gate and regional coverage; open symbols mark partial months. (c) Gate-to-weighted-comparison coverage ratios on 1264 orbit-paired dates during July 2021-December 2024, for CH_4, standard-quality CO and clear-sky/clear-sky-like CO. Non-gate weights balance mean latitude, longitude and elevation. Whiskers show 95% intervals from a 28-calendar-day circular block bootstrap; the dashed line denotes equal coverage. (d) Weighted CH_4 processing-status distributions among native pixels matched to valid clear-sky/clear-sky-like CO observations. Fractions are standardized across supported cell-days and cells. Screening, matching and weighting procedures are described in Supplementary Note 7.

Discussion

The observation-constrained Shanxi inventory gives the source-receptor analysis an empirical foundation in both satellite columns and measured methane fluxes[17]. Coupling this source information to

WRF-GHG reveals how its downwind expression changes as circulation connects the coal basins to the North China Plain. The 3.36-fold amplification under sustained southwesterly flow shows that the regional consequence of source refinement can be substantially greater during favorable transport conditions than its period-mean response suggests. Studies of CO transport from the Guanzhong Basin[20] and southern Africa[33], and BC export from continental Southeast Asia[34], likewise demonstrate how circulation and vertical redistribution connect concentrated emissions to distant receptors. Methane inversions over South Asia further show how transport and observing-network coverage shape regional emission constraints[35]. Our results extend this source-receptor perspective in a mountainous industrial airshed, where the location of emissions relative to ventilation pathways determines how changes in source representation are expressed across administrative boundaries.

The "leaky bathtub" analogy captures the coexistence of local accumulation and terrain-guided ventilation[8]. The three-dimensional diagnostics give this interpretation a physical expression in the Shanxi-BTH system. Along the northern transect, an anthropogenic enhancement progresses coherently towards the Beijing-Xianghe sector. Along the southern transect, enhancements develop as intermittent pulses from the Changzhi coal basin towards the BTH receptor region. Their along-path evolution occurs within a vertically structured flow, with methane-rich lower layers contributing strongly to the enhanced columns (Figs. 4-5). These configurations expose different parts of the plain to the upwind source region. Beijing lies within the principal northern footprint of EOF1 and near the northern margin of the southern EOF3 configuration. The broader EOF3 loading extends across southern Hebei into Shandong, beyond the receptor region used for the mass-response calculation. This asymmetry gives a geographical basis for observing both pathways and extending the receptor perspective beyond Beijing.

The observational evaluations are central to interpreting the consequences of inventory refinement. The flux-constrained source field is examined through source-region COCCON columns[36], the Xianghe receptor record and the background and farther-field comparisons (Supplementary Note 5). These measurements test different parts of the emission-transport-column relationship, providing checks that a single receptor comparison cannot supply. They also show why agreement in mean concentration and agreement at selected high-column timestamps need not improve together. Residual source-region offsets, considered alongside the inventory evaluation[17] and published sensitivity assessments[37], motivate the coherent 10-30% source-scale sensitivity range applied to the Shanxi inventory-refinement increment. Under this analytical rescaling, absolute responses change proportionally and the common factor cancels from the amplification ratio. Spatial heterogeneity has a different signature: the fixed-seed ±50% experiment produces an August-mean BTH response of only 60.7 tons alongside hourly excursions reaching 24.4×10^3 tons. Resolving source locations therefore matters even when positive and negative responses largely cancel in the period mean. Together, the evaluations and sensitivity analyses establish why source magnitude, spatial allocation and atmospheric transport must be considered jointly when interpreting receptor agreement.

The model period 1-2-day ordering gains broader context from the positive +1-day PC1-PC3 association in the satellite-native record beyond 2022 (Fig. 9). Persistent Xianghe associations likewise extend the receptor relevance of the regional configurations beyond the simulated summer. Their significance for verification follows from the pronounced response during brief periods of favorable circulation. Short campaigns can undersample these conditions, while temporal averaging smooths individual enhancements and obscures their relationship to the evolving flow. Cohen's analysis of Southeast Asian fire-related aerosols similarly illustrates how broad regional averages can conceal spatially distinct patterns of variability[38]. Long records retain the context needed to distinguish an isolated

enhancement from a recurring atmospheric relationship. Interpreting those records at the timescales of transport preserves information about when an upwind source change becomes visible at a receptor, complementing monthly provincial emission assessments[39].

Coal-mine methane provides a complementary long-lived indicator of atmospheric organization within North China's aerosol-rich industrial airshed, where fugitive extraction emissions coexist with combustion sources. At Xianghe, the coherent positive associations of XCH_4, XCO and XCO_2 with AOD over more than 500 common days provide strong support to place the methane receptor signal within a broader multipollutant context involving combustion-related trace gases and aerosol loading[18,19,28,40](Fig. 7e; Fig. S21). Shared direct-sun retrievals leave atmospheric covariance and residual optical-path sensitivity partly inseparable. All three regional modes retain positive Xianghe associations after AOD adjustment and exclusion of 2022 (Fig. S22). The tested event-level aerosol scenarios also yield similar overall magnitude-capture fractions, while the 4 August amplitude remains potentially aerosol-sensitive (Fig. S23). These results give the methane analysis relevance to the wider challenge of observing industrial air masses over North China and motivate coordinated gas and aerosol measurements along their regional transport connections.

The long record also reveals a sharp mismatch between transport geography and satellite sampling. The CH_4-CO comparison links this mismatch to terrain-dependent methane screening, showing how a model-diagnosed transport corridor can remain poorly represented even where the same instrument retrieves another trace gas (Fig. 10). A regional coverage statistic thus conceals a much more severe local gap along a model-diagnosed pathway. Because these gate cells fall outside the satellite EOF coverage mask, the long-record analysis constrains surrounding atmospheric organization and receptor expression while providing little direct evidence of passage through the gate. The consequences of observation selection extend to emission estimation[41]. Comparisons of European inversions using different TROPOMI products demonstrate that coverage and error characterization affect the resulting regional budgets[23]. In the Taihang setting, the persistent gap identifies a specific part of the source-receptor connection where complementary measurements could strengthen the observational constraint.

The pathway geometry provides a practical starting point for such monitoring. Zhoukoudian would sample an intermediate position within the northern EOF1 footprint between Shanxi and Xianghe, while Dezhou would extend observations into the southern EOF3 lobe towards Shandong. The model-derived 149 km horizontal forecast-error correlation length supplies an initial spatial constraint for evaluating these locations (Supplementary Note 7). Instrument footprints, local representativeness and transport conditions beyond the simulated summer would also inform network design. Measurements spanning both configurations would help determine how their different geographical expressions contribute to variability across the wider airshed. For future satellite missions, effective methane coverage of transport pathways should be evaluated alongside regional observed-area fraction. The CH_4-CO contrast underscores the need to assess pathway-specific retrieval availability when translating satellite sampling characteristics into MRV network design (Supplementary Note 8).

The quantitative scope of the study is set by the 1608-h simulation during summer 2022. Its conditional mass responses describe the amplification attained under the sampled atmospheric states; their seasonal variation and contribution to an annual budget require corresponding mass-response calculations. The multiyear observations already extend the assessment of regional organization and receptor expression beyond that summer. Absolute response magnitudes remain sensitive to the adopted source field, as examined through coherent rescaling and the spatial-heterogeneity experiment. Near individual mines, retrieval footprints and model-grid representativeness also complicate point-scale

evaluation, placing the regional column-mass response on a different spatial footing from facility-level agreement. Finally, the upper-bound OH calculation gives approximately 1% methane loss over 7-10 days[42], supporting the passive-tracer approximation over the transport timescales examined here (Supplementary Note 6).

These findings place cross-boundary methane verification within an episode-resolved source-gate-receptor framework. Observation-constrained inventories establish the source representation, atmospheric-state diagnostics identify when and where its downwind influence is amplified, and coverage analysis reveals which parts of that connection remain weakly observed. This approach offers a basis for coordinated verification across the Shanxi-BTH airshed and has wider relevance to methane-control efforts under China's Ecological and Environmental Code[25] and international initiatives such as the Global Methane Pledge. The Indo-Gangetic Plain, continental Southeast Asia and southern Africa offer further settings in which to apply and test the framework, wherever concentrated emissions, complex terrain and administrative boundaries create comparable source-receptor mismatches. Effective atmospheric verification depends on observing the connections between jurisdictions as well as the emissions within them.

Methods

WRF-GHG model configuration

The greenhouse gas simulations were conducted with the WRF-GHG model, a greenhouse-gas configuration of the WRF-Chem (Weather Research and Forecasting model with Chemistry) framework[43-46]. Under this configuration, CO_2, CH_4, and CO were treated as passive tracers, with emissions, advection, convection and turbulent mixing represented but gas-phase chemical production and loss omitted to focus on their transport dynamics. We evaluated the CH_4-tracer approximation using a conservative OH loading and found the estimated loss is under 1.1% over the longest transport duration considered, as explained in detail in Supplementary Note 6.

To balance spatial resolution and computational efficiency, a three-level nested grid system (outer: 27 km, middle: 9 km, and inner: 3 km) based on Lambert projection coordinates was implemented, covering the study region and its surrounding areas (Fig. S9). All domains used 60 eta vertical levels (59 mass levels) extending from the surface up to 50 hPa, ensuring sufficient resolution to capture both boundary-layer and lower free troposphere transport of GHGs[47]. Physical parameterization options are summarized in Table S5.

The simulations covered 1 July to 16 September 2022. Based on sensitivity tests of tracer-field stabilization, the first nine days were excluded, and the primary attribution analysis used 1608 consecutive hourly outputs from 00:00 UTC on 10 July through 00:00 UTC on 15 September 2022. Model output was archived hourly for the baseline configurations and at 30-min intervals for selected perturbation configurations. All paired differences were calculated at identical UTC timestamps. The EOF decomposition used the full 1645-h XCH_4 record from 00:00 UTC on 10 July through 12:00 UTC on 16 September 2022, whereas all ΔM analyses used the 1608-h common-response window defined above.

Initial and boundary conditions (IC/BC)

Meteorological and methane-tracer initial and boundary conditions were specified independently. Meteorological initial and lateral boundary conditions were generated from the ECMWF ERA5 reanalysis fields[48,49] using the WRF Preprocessing System and supplied to WRF at 3-h intervals. Each daily simulation cycle comprised a 6-h ERA5-constrained meteorological spin-up from 18:00 UTC on

the preceding day to 00:00 UTC, followed by a 24-h production integration. The first cycle was initialized as a cold start. In subsequent cycles, the accumulated greenhouse-gas tracer fields were transferred through restart files to retain their transport history across the daily meteorological cycling[21,50,51]. ERA5 therefore constrained the simulated transport through the meteorological initialization and outer-domain lateral boundary conditions[52]. Background methane was prescribed from 6-hourly CESM2.2/CAM-Chem output[53], which was interpolated to the WRF-GHG grid to initialize the CH_4 background tracer and provide time-varying lateral boundary conditions for the outermost domain.

A priori inventory

Three sector-specific emission inventories were used to quantify anthropogenic (ANT), biogenic (BIO), and biomass burning (BBU) sources of CH_4. For anthropogenic emissions, the primary dataset was the EDGAR_2024_GHG[24], which provided monthly global emissions (energy, industry, waste sectors) at 0.1°×0.1° resolution; this was supplemented by an observation-constrained model-free mass conservation dataset[17,18,22] for Shanxi's coal-mining regions, to refine coal-related emissions. For biogenic emissions (wetland CH_4), the WetCHARTs v1.3.3 dataset[54] was adopted with 0.5°×0.5° spatial and monthly temporal resolution. For biomass burning emissions (wildfires, agricultural burning), data came from FINN v2.5[55], which provides gridded CH_4 emissions at 0.1°×0.1° resolution using MODIS fire radiative power (FRP) observations. The a priori emission fields are compared in Supplementary Note 2.

TCCON station data and other auxiliary data

TCCON Fourier-transform spectrometers retrieve precise column-averaged dry-air mole fractions of CO_2, CH_4, N_2O and CO from direct-sun near-infrared spectra[21,56]. Xianghe observations (39.80°N, 116.96°E; 30m a.s.l.), which provide the primary BTH receptor record, were obtained from the GGG2020.R0 product[56] (https://doi.org/10.14291/tccon.ggg2020.xianghe01.R0). Published documentation for the Xianghe record reports that spectra obtained under high-aerosol or cloudy conditions are screened using the stability of the interferogram direct-current signal, with spectra showing variations greater than 5% excluded before retrieval[28]. All simulation-observation bias and RMSE statistics at Xianghe are computed over TCCON-retrieval hours after removal of 99.9th-percentile z-score outliers. The source-to-receptor evaluation additionally uses paired EM27/SUN columns at the southeastern Shanxi supersite[36], Hefei TCCON GGG2020.R1 columns[57] (31.91°N, 117.17°E; https://doi.org/10.14291/tccon.ggg2020.hefei01.R1) as a far-field comparison, and the Waliguan background record[58] (Supplementary Note 5).

The ground-based AOD observations utilized in this study were acquired from the Aerosol Robotic Network (AERONET)[59]. The provincial administrative boundary data used in this study were from China's official national geospatial information service platform, with the official Map Review Number: GS (2024) 0650, adhering to national regulatory requirements, publicly available at https://www.tianditu.gov.cn/. The Digital Elevation Model (DEM) data were derived from the Shuttle Radar Topography Mission (SRTM) V4.1 dataset[60], publicly available at https://earthexplorer.usgs.gov/. The data were clipped, resampled and projected to match the nested model domains. Terrain roughness was calculated on the gridded elevation field as the magnitude of its local row and column gradients.

Daily Copernicus Sentinel-5P/TROPOMI operational Level-2 XCH_4 retrievals acquired from 1 July 2021 through 1 January 2026 were obtained from the Copernicus Data Space Ecosystem[61,62]. We retained land retrievals with QA value $\geq$ 0.5 and processor version 2.0.0 or later. Where multiple processor versions were available for the same orbit, the most recent valid product was retained. The screened retrievals were aggregated into daily fields on the common 9-km Lambert grid. Grid cells with valid

observations on fewer than 10% of the analysis days were excluded from the EOF domain, leaving 4618 common finite cells. Missing values in the daily anomaly matrix used for EOF estimation were reconstructed with DINEOF[63]; rank 29 minimized prediction error on a withheld 2% validation set. Reconstructed values were used only for EOF estimation, while retrieval-coverage and terrain-gate observability calculations used the raw final-QC observation mask.

Calendar lags were evaluated by pairing PC1 on day t with PC3 on day t + lag only when both dates were present. Lagged-correlation intervals were estimated from 2000 circular moving-block bootstrap replicates with 14-calendar-day blocks. Daily Xianghe means were calculated from TCCON retrievals between 04:00 and 07:00 UTC that satisfied 0.96 ≤ xluft ≤ 1.04 and solar zenith angle ≤ 75°, and were matched to TROPOMI PCs by calendar date. The joint receptor model included PC1, PC2, PC3, season and year; Fig. 9c intervals were obtained from 2000 circular moving-block bootstrap replicates with 28-calendar-day blocks.

Calculation of column-averaged methane (XCH_4)

The ideal gas law ($PV = nRT$) was used to calculate the dry-air molar density (ρ_{da}, unit: mol·m^{-3}):

$$\rho_{\mathrm{da}} = \frac{P_{\mathrm{total}}}{R \cdot T_{\mathrm{abs}}} \cdot \frac{1}{1+1.6075 q_v} \tag{1}$$

where total atmospheric pressure (P_{total}) is the sum of perturbation pressure (P) and base-state pressure (PB); R = 8.3145 J·mol^{-1}K^{-1} is the universal gas constant; absolute temperature (T_{abs}) was converted from potential temperature (T) via $T_{\mathrm{abs}} = (T + 300) \times (P_{\mathrm{total}}/P_0)^{0.2865}$ and q_v is the water vapor mixing ratio. The factor ($1+1.6075\, q_v$) applies the water-vapor correction in the dry-air density calculation. Column-averaged methane was then calculated by density-weighted vertical integration:

$$\mathrm{XCH_4} = \frac{\sum_{l=1}^{n-1} \mathrm{CH_4}(l) \cdot \rho_{\mathrm{da}}(l) \cdot \Delta z(l)}{\sum_{l=1}^{n-1} \rho_{\mathrm{da}}(l) \cdot \Delta z(l)} \tag{2}$$

where $\mathrm{CH_4}(l)$ is the total CH_4 mixing ratio (ppbv) at level l; and n is the vertical layer. Layer thickness (Δz, units: m) was calculated from adjacent physical height levels as $\Delta z(l) = z_{l+1} - z_l$, where l denotes the vertical level. Physical height (z_l) was calculated as $\frac{\mathrm{PH}_l + \mathrm{PHB}_l}{g}$, using geopotential height variables PH and PHB, with g as gravitational acceleration. The density-weighted integration therefore uses the modelled pressure, temperature, water-vapour content and geometric thickness of each layer.

Terrain-XCH_4 coupling

The Terrain-XCH_4 Coupling Index is a descriptive product of standardized elevation and gridded XCH_4. It was calculated in two steps:

$$\mathrm{proxy}_{\mathrm{norm}}(x, y) = \frac{\mathrm{proxy}(x,y) - \mu_{\mathrm{proxy}}}{\sigma_{\mathrm{proxy}}} \tag{3}$$

where $\mathrm{proxy}(x, y)$ denotes elevation (m) or XCH_4 (ppbv) at the grid cell (x, y), and μ_{proxy} denotes the spatial mean of the elevation or XCH_4 field across the SX-BTH domain, and σ_{proxy} denotes its spatial standard deviation.

The Terrain-XCH_4 Coupling Index for each grid cell (x, y) is the element-wise product of the standardized elevation and XCH_4 fields:

$$C(x, y) = \mathrm{DEM}_{\mathrm{norm}}(x, y) \times \mathrm{XCH_4}_{\mathrm{norm}}(x, y) \tag{4}$$

The sign indicates whether standardized elevation and XCH_4 anomalies have the same or opposite sign at a grid cell, and the magnitude is their local product. The index serves as a spatial screening field; the EOF and three-dimensional diagnostics provide its transport interpretation.

Empirical orthogonal function (EOF)-based decomposition of spatiotemporal variability

To extract the dominant modes of spatiotemporal variability in XCH_4 across the SX-BTH region, we employed empirical orthogonal function (EOF) analysis, which is a principal component-based decomposition technique widely used for disentangling high-dimensional spatiotemporal datasets[19]. The input comprised gridded WRF-GHG Top-down XCH_4. Each grid-cell time series was linearly detrended and standardized before decomposition to ensure the focus was on intrinsic XCH_4 variability.

The EOF decomposition accounted for non-uniform grid-cell areas on the Lambert conformal grid. We therefore integrated grid-area weighting into the EOF constructor: each grid cell's XCH_4 time series was multiplied by the square root of its geographic area (calculated via WRF's projection parameters and grid corner coordinates) before covariance matrix computation, so that the resulting modes are not distorted by grid geometry.

The decomposition yields mutually orthogonal spatial loadings and temporal coefficients, ordered by explained variance (see Cohen, 2014[38]). We retained EOF1, EOF2 and EOF3 in the regional decomposition. The North et al.[64] criterion was used to assess eigenvalue separation; because the sampling-error ranges for EOF2 and EOF3 overlap in the short model record, both modes were retained. EOF1 and EOF3 define the broad synoptic and terrain-sensitive diagnostic transects, and EOF2 is included in the all-mode receptor analyses. For the model-satellite comparison, centered and area-weighted TROPOMI EOF2 was projected onto the model EOF2-EOF3 subspace over 4618 common cells. Spatial confidence intervals were obtained from 2000 resamples of 55 contiguous geographic blocks. For the complementary model-pattern test, the signed WRF-GHG EOF1-EOF3 fields shown in Fig. 4 were fitted jointly to each daily standardized TROPOMI anomaly field using only original observed cells shared by the two products; DINEOF-filled cells were excluded. The projected coefficients were standardized over the full record and entered into the same joint receptor model.

Terrain-gate observability analysis

The fixed terrain gate was delineated from the model-derived PC1 Terrain-XCH_4 field independently of satellite availability. Coverage used original final-QC retrievals, excluding DINEOF-filled values, with monthly means calculated over all calendar days. Entropy weights balanced mean latitude, longitude and elevation between the gate and eligible non-gate cells.

CH_4-CO coverage was compared on the same 9-km grid on 1264 orbit-paired dates during July 2021-December 2024, retaining processor versions ≥2.2.0. Native-pixel diagnostics matched orbit, observation time and ground-pixel identifier, requiring pixel centers within 1 km and common land and viewing-geometry restrictions. CH_4 processing statuses were summarized conditional on valid clear-sky/clear-sky-like CO, with fractions averaged within cell-days, across days and then across cells. Coverage intervals used 2000 circular moving-block bootstrap replicates with 28-calendar-day blocks, paired across products for the CH_4-CO comparison. Screening thresholds, supported-cell weighting and spatial sensitivity analyses are detailed in Supplementary Note 7.

NMC method

The spatiotemporal heterogeneity of methane concentration uncertainties was characterized using the NMC method (Parrish & Derber, 1992[65]) based on WRF-GHG Top-down samples. Forecast-difference values outside the pooled 1st-99th percentile range were excluded before horizontal correlations were fitted[66]. The covariance was estimated from differences between 48-h and 24-h forecasts valid at the same time throughout August 2022. The analysis resolves the horizontal decorrelation length scale and vertical error structure.

Horizontal correlations were assumed vertically homogeneous, horizontally isotropic, and fitted by a one-dimensional Gaussian function. For any two horizontal grid points x_1 and x_2, the correlation is

expressed as:

$$C_x = e^{\left[-\frac{(x_1-x_2)^2}{2L_x^2}\right]}, \quad (5)$$

where L_x denotes the horizontal decorrelation length scale, defined as the distance at which the correlation falls to $e^{-1/2}$, and estimated from model data. The vertical correlation matrix C_z was directly calculated from model forecasts using the NMC method[65]. The larger the horizontal decorrelation length scale, the farther observational information propagates horizontally, and the broader its impact on the background field. Sampling-error calculations and the model-satellite structural analyses are detailed in Supplementary Note 3.

Attribution experiment design and column mass quantification

We designed five simulation configurations to quantify downwind methane-column responses to the refined Shanxi source field, specified regional emission reductions and source-field perturbations. All paired differences were evaluated at exact common UTC timestamps.

Experiment definitions. The five simulations are:

(1) EDGAR: baseline simulation driven by the standard EDGAR_2024_GHG inventory[24].

(2) Top-down: refined simulation where emissions from coal mine grids in Shanxi Province are replaced with the satellite-constrained high-resolution inventory of Hu et al. (2024)[17].

(3) Perturb±10%/±50%: with Shanxi coal mine emissions randomly perturbed by ±10% or ±50% on a per-grid-cell basis to provide a broad, reproducible source-heterogeneity stress test. Per-grid perturbation factors were drawn from a uniform distribution using a fixed random seed, ensuring full reproducibility of the reported Δ_{SX} statistics.

(4) BTH-50%: with anthropogenic emissions throughout BTH uniformly reduced by 50%.

(5) BJ-50%: with anthropogenic emissions within Beijing municipality uniformly reduced by 50%.

The Perturb±10%/±50%, BTH-50% and BJ-50% configurations used the Top-down emission configuration as their inventory baseline and were integrated separately with the specified emission modifications. Signed differences were evaluated at exact common UTC timestamps and are interpreted as same-time scenario contrasts.

Derived response metrics. Pairwise response fields were calculated only at exact common UTC timestamps.

(1) Δ_{inv} = Top-down − EDGAR represents the change in simulated methane columns produced by replacing the EDGAR Shanxi coal-mine field with the observation-constrained inventory under identical meteorology.

(2) Δ_{SX} = Perturb±50% − Top-down: represents the response to the spatially heterogeneous ±50% Shanxi source-field perturbation.

(3) Δ_{BTH} = Top-down − BTH-50% represents the response to a 50% reduction in anthropogenic emissions throughout BTH.

(4) Δ_{BJ} = Top-down − BJ-50% represents the response to a 50% reduction in Beijing anthropogenic emissions.

(5) $\Delta_{TH} = \Delta_{BTH} - \Delta_{BJ}$ is the algebraic Tianjin-Hebei residual.

Because Δ_{TH} is defined as $\Delta_{BTH} - \Delta_{BJ}$, the corresponding mass-response series was calculated after mass conversion as $\Delta M_{TH} = \Delta M_{BTH} - \Delta M_{BJ}$. For each paired contrast, dry-air column density (N_{dry}) was taken from the second, subtracted simulation: EDGAR for Δ_{inv}, Top-down for Δ_{SX}, BTH-50% for Δ_{BTH}, and BJ-50% for Δ_{BJ}.

Conversion from ΔXCH_4 to column mass response (ΔM). The difference in column-averaged

dry-air mole fraction (ΔXCH_4, in ppbv) was converted to an integrated column mass anomaly (ΔM, in tons) over a specified geographic region R using dry-air column density (N_{dry}) from the corresponding subtrahend simulation:

$$\Delta \mathrm{M}_R(t) = \sum_{i,j\in R}\left[\Delta \mathrm{XCH_4}(i,j,t) \times 10^{-9} \times N_{\mathrm{dry}}(i,j,t) \times M_{\mathrm{CH_4}} \times A_{i,j}\right]/1000 \quad (6)$$

where $\Delta \mathrm{XCH_4}(i,j,t)$ is the concentration difference at grid cell (i,j) and time t (units: ppbv); $N_{\mathrm{dry}}(i,j,t)$ is the vertically integrated dry-air column density (units: mol m^{-2}), computed from the corresponding subtracted simulation's pressure, temperature, and water vapor fields (see Eq. (1) and (2)); $M_{\mathrm{CH_4}}$ is the molar mass of methane; $A_{i,j}$ is the geographic area of the grid cell, calculated from the Lambert projection parameters, and administrative masks were evaluated on the native two-dimensional XLAT and XLONG coordinates.

Stratification by EOF modes. To assess meteorological modulation, the $\Delta \mathrm{M_{inv}}$ time series was stratified by normalized principal-component amplitudes N1=PC1/σ_{PC1} and N3=PC3/σ_{PC3}. Thresholds of ±1.5, ±2.0, ±2.5, and ±3.0 were applied to define periods of strong positive/negative phase for each EOF mode, as well as their concurrent occurrences. Mean $\Delta \mathrm{M_{inv}}$ was calculated for each subset to quantify amplification or suppression of the paired inventory-refinement response under specific atmospheric states.

Validation using tower-based observations of CH_4 flux in Shanxi. Open-path CH_4, CO_2/H_2O and three-dimensional wind were measured at 10 m at DaBuTou, within the active Shanxi coal-mining region, using an LI-7700 analyzer and an IRGASON system. Thirty-minute CH_4 fluxes were calculated by eddy covariance with the Webb-Pearman-Leuning correction. The observed fluxes are of the same order as the collocated Top-down prior emission at the grid in which they were measured, while they are approximately an order of magnitude above EDGAR. This has been further confirmed in a ground study by Lu et al.[67], which also inverted emissions from this same grid as source A. These independent observations support the scale and proper spatial-temporal location of the Shanxi coal-mine source used in Δ_{inv} and the broader Δ_{SX} sensitivity test. Details are provided in Supplementary Note 2.

Peak-event definition and reproduction metric. Candidate timestamps were defined as local maxima above the 90th percentile of observed XCH_4 in each matched observation sequence. Successive candidates were separated by at least 12 valid retrieval records in the hourly product and 24 valid records in the nominal 30-min product. Both selections yielded ten timestamps, with a minimum realized clock-time separation of 49 h. A timestamp met the one-sided magnitude criterion when simulated XCH_4 reached at least 99% of the observed value. The complete peak-selection and matching procedure was repeated for each aerosol diagnostic scenario rather than applying a correction to a fixed set of events. The fixed timestamps and event-definition sensitivity are reported in Supplementary Note 4, Tables S2-S3 and Fig. S23c.

Aerosol sensitivity analysis. Direct-sun AERONET AOD measurements at Xianghe were used to evaluate aerosol-related covariance in the TCCON XCH_4 comparison. The observed AOD-XCH_4 association was treated as a combined atmospheric and retrieval-sensitivity diagnostic without a unique causal partition. The direct AOD-XCH_4 analysis comprised 678 overpass-window days. Cross-species analyses used 533 days common to deseasonalized XCH_4, XCO, XCO_2 and AOD. Native-unit cross-species slopes and their 95% intervals were estimated using Newey-West covariance with seven retained-observation lags. For Fig. 7e, the slopes were normalized by the standard deviation of each gas anomaly, while AOD_{440} remained on its native scale. An xluft-based path-length calculation and an independent within-day calculation yielded XCH_4 sensitivity coefficients spanning +0.53 to +19.8 ppb AOD^{-1}. Event selection and magnitude matching were repeated for every adjusted observation series. On the same 533

common days, deseasonalized Xianghe XCH_4 was regressed jointly on standardized AOD_{440}, PC1, PC2 and PC3, with season and year included as categorical covariates. The PC scores retained their full-record standardization, while AOD_{440} was standardized over the 533-day common record before cohort selection. Confidence intervals for the 678-day AOD-XCH_4 association and the reported receptor-model coefficients were estimated from 2000 circular moving-block bootstrap replicates using 28-calendar-day blocks. The equations and reference states used to construct the adjusted XCH_4 series are provided in Supplementary Note 4.

Data availability

The ERA5 reanalysis product is available at https://doi.org/10.24381/cds.bd0915c6. The CESM2/CAM-chem product can be accessed from https://www.acom.ucar.edu/cesm. The EDGAR_2024_GHG product is available at https://edgar.jrc.ec.europa.eu/dataset_ghg2024. The CMM dataset can be accessed from https://figshare.com/s/73ef139b4b896dfa79a7. The FINN v2.5 product is available at https://gdex.ucar.edu/datasets/d312009/. The WetCHARTs v1.3.3 dataset is available at https://doi.org/10.3334/ORNLDAAC/2346. Xianghe TCCON GGG2020.R0 and Hefei TCCON GGG2020.R1 data are available at https://doi.org/10.14291/tccon.ggg2020.xianghe01.R0 and https://doi.org/10.14291/tccon.ggg2020.hefei01.R1, respectively. AERONET Version 3 Level 1.5 observations are available from https://aeronet.gsfc.nasa.gov/. Copernicus Sentinel-5P/TROPOMI Level-2 methane total-column products are available through the Copernicus Data Space Ecosystem (https://dataspace.copernicus.eu/) and are described by the Version 02 product record at https://doi.org/10.5270/S5P-3lcdqiv. TROPOMI Level-2 carbon monoxide total-column products, Version 02, were obtained from the same archive (https://doi.org/10.5270/S5P-bj3nry0). The data that support the findings of this study are openly available at the following URL/DOI: https://figshare.com/s/c31984e75e906cbc6e82.

Code availability

The code is available in the Figshare database (https://figshare.com/s/c31984e75e906cbc6e82).

References

1 Jacob, D. J. et al. Quantifying methane emissions from the global scale down to point sources using satellite observations of atmospheric methane. *Atmos. Chem. Phys.* **22,** 9617–9646 (2022).

2 Estrada, L. A. et al. Integrated Methane Inversion (IMI) 2.0: an improved research and stakeholder tool for monitoring total methane emissions with high resolution worldwide using TROPOMI satellite observations. *Geosci. Model Dev.* **18,** 3311–3330 (2025).

3 World Meteorological Organization. *The State of Greenhouse Gases in the Atmosphere Based on Global Observations through 2024*. WMO Greenhouse Gas Bulletin No. 21 (WMO, Geneva, 2025).

4 IPCC. *Climate Change 2023: Synthesis Report. Contribution of Working Groups I, II and III to the Sixth Assessment Report of the Intergovernmental Panel on Climate Change* (eds Core Writing Team, Lee, H. & Romero, J.) (IPCC, Geneva, 2023).

5 International Energy Agency. *Driving Down Coal Mine Methane Emissions* (IEA, Paris, 2023).

6 Peng, S. et al. High-resolution assessment of coal mining methane emissions by satellite in Shanxi, China. *iScience* **26,** 108375 (2023).

7 Han, G. et al. Unveiling unprecedented methane hotspots in China's leading coal production hub:

a satellite mapping revelation. *Geophys. Res. Lett.* **51,** e2024GL109065 (2024).
8 Lu, R. & Turco, R. P. Air pollutant transport in a coastal environment—II. Three-dimensional simulations over Los Angeles basin. *Atmos. Environ.* **29,** 1499–1518 (1995).
9 Tianjin Municipal Bureau of Ecology and Environment. *Action Plan for Methane Emission Control of Tianjin*. Jin Huan Qi Hou [2024] No. 34 (2024) [in Chinese].
10 Beijing Municipal Bureau of Ecology and Environment. *Action Plan for Methane Emission Control of Beijing*. Jing Huan Fa [2025] No. 9 (2025) [in Chinese].
11 Ministry of Ecology and Environment of the People's Republic of China. *Methane Emissions Control Action Plan*. Huan Qi Hou [2023] No. 67 (2023) [in Chinese].
12 Hancock, S. E. et al. Satellite quantification of methane emissions from South American countries: a high-resolution inversion of TROPOMI and GOSAT observations. *Atmos. Chem. Phys.* **25,** 797–817 (2025).
13 Shen, L. et al. National quantifications of methane emissions from fuel exploitation using high resolution inversions of satellite observations. *Nat. Commun.* **14,** 4948 (2023).
14 Zhong, H. et al. Quantifying methane emission baselines with high-resolution satellite data to support China's emission control. *Sci. Bull.* **70,** 2255–2259 (2025).
15 Sheng, J., Song, S., Zhang, Y., Prinn, R. G. & Janssens-Maenhout, G. Bottom-up estimates of coal mine methane emissions in China: a gridded inventory, emission factors, and trends. *Environ. Sci. Technol. Lett.* **6,** 473–478 (2019).
16 Zhang, J., Qiu, B., Khanna, N. & Lin, J. Regional production shift and increased utilization dampen the growth of China's coal mine methane emissions. *Commun. Earth Environ.* **6,** 964 (2025).
17 Hu, W., Qin, K., Lu, F., Li, D. & Cohen, J. B. Merging TROPOMI and eddy covariance observations to quantify 5-years of daily CH_4 emissions over coal-mine dominated region. *Int. J. Coal Sci. Technol.* **11,** 56 (2024).
18 Li, X. et al. Space-based inversion reveals underestimated carbon monoxide emissions over Shanxi. *Commun. Earth Environ.* **6,** 357 (2025).
19 Tiwari, P. et al. Multi-platform observations and constraints reveal overlooked urban sources of black carbon in Xuzhou and Dhaka. *Commun. Earth Environ.* **6,** 38 (2025).
20 Wang, S. et al. Synergistic analysis and vertical transport attribution of carbon monoxide surface concentrations and satellite column loadings over China. *Remote Sens. Environ.* **344,** 115562 (2026).
21 Callewaert, S. et al. A WRF-Chem study of the greenhouse gas column and in situ surface concentrations observed in Xianghe, China – Part 1: methane (CH_4). *Atmos. Chem. Phys.* **25,** 9519–9544 (2025).
22 Zheng, B. et al. How can we trust TROPOMI based methane emissions estimation: calculating emissions over unidentified source regions. *Atmos. Chem. Phys.* **26,** 1931–1946 (2026).
23 Sicsik-Paré, A. et al. Assessment of the differences in European CH_4 emission estimates from three TROPOMI products. *Atmos. Chem. Phys.* **26,** 10423–10454 (2026).
24 Crippa, M. et al. *GHG Emissions of All World Countries*. JRC138862 (Publications Office of the European Union, Luxembourg, 2024).
25 National People's Congress of China. *Ecological and Environmental Code of the People's Republic of China* (2026) [in Chinese].
26 Cohen, J. B., Prinn, R. G. & Wang, C. The impact of detailed urban-scale processing on the composition, distribution, and radiative forcing of anthropogenic aerosols. *Geophys. Res. Lett.* **38,**

L10808 (2011).
27 Blumenthal, D. L., White, W. H. & Smith, T. B. Anatomy of a Los Angeles smog episode: pollutant transport in the daytime sea breeze regime. *Atmos. Environ.* **12,** 893–907 (1978).
28 Han, P. et al. Spatiotemporal variations in atmospheric CH_4 concentrations and enhancements in northern China based on a comprehensive dataset: ground-based observations, TROPOMI data, inventory data, and inversions. *Atmos. Chem. Phys.* **25,** 4965–4988 (2025).
29 Guan, L. et al. Improving aerosol absorption estimates via size-resolved constraints based on AERONET and in situ measurements. *Geophys. Res. Lett.* **53,** e2025GL117418 (2026).
30 Wang, S., Wang, X., Cohen, J. B. & Qin, K. Inferring polluted Asian absorbing aerosol properties using decadal scale AERONET measurements and a MIE model. *Geophys. Res. Lett.* **48,** e2021GL094300 (2021).
31 Guan, L. et al. In-tandem multi-waveband particulate absorption and size observations yield substantial changes in radiative forcing over industrial Central China. *Atmos. Chem. Phys.* **26,** 3107–3123 (2026).
32 Wang, D. et al. A three-dimensional variational data assimilation system for a size-resolved aerosol model: implementation and application for particulate matter and gaseous pollutant forecasts across China. *Sci. China Earth Sci.* **63,** 1366–1380 (2020).
33 Lin, C., Cohen, J. B., Wang, S., Lan, R. & Deng, W. A new perspective on the spatial, temporal, and vertical distribution of biomass burning: quantifying a significant increase in CO emissions. *Environ. Res. Lett.* **15,** 104091 (2020).
34 Wang, S., Cohen, J. B., Deng, W., Qin, K. & Guo, J. Using a new top-down constrained emissions inventory to attribute the previously unknown source of extreme aerosol loadings observed annually in the Monsoon Asia free troposphere. *Earth's Future* **9,** e2021EF002167 (2021).
35 Belikov, D. A. et al. Assessment of the impact of observations at Nainital (India) and Comilla (Bangladesh) on the CH_4 flux inversion. *Prog. Earth Planet. Sci.* **11,** 36 (2024).
36 Tu, Q., Hase, F., Qin, K., Alberti, C. & Lu, F. COCCON measurements of XCO_2, XCH_4 and XCO over coal mine aggregation areas in Shanxi, China, and comparison to TROPOMI and CAMS datasets. *Remote Sens.* **16,** 4022 (2024).
37 Maasakkers, J. D. et al. Using satellites to uncover large methane emissions from landfills. *Sci. Adv.* **8,** eabn9683 (2022).
38 Cohen, J. B. Quantifying the occurrence and magnitude of the Southeast Asian fire climatology. *Environ. Res. Lett.* **9,** 114018 (2014).
39 Cui, D. et al. Monthly methane emissions in Chinese mainland provinces from 2013–2022. *Sci. Data* **12,** 948 (2025).
40 Wang, S., Cohen, J. B., Lin, C. & Deng, W. Constraining the relationships between aerosol height, aerosol optical depth and total column trace gas measurements using remote sensing and models. *Atmos. Chem. Phys.* **20,** 15401–15426 (2020).
41 Qu, Z. et al. Global distribution of methane emissions: a comparative inverse analysis of observations from the TROPOMI and GOSAT satellite instruments. *Atmos. Chem. Phys.* **21,** 14159–14175 (2021).
42 Burkholder, J. B. et al. *Chemical Kinetics and Photochemical Data for Use in Atmospheric Studies, Evaluation No. 20*. JPL Publication 25-1 (Jet Propulsion Laboratory, Pasadena, CA, 2025).
43 Grell, G. A. et al. Fully coupled "online" chemistry within the WRF model. *Atmos. Environ.* **39,** 6957–6975 (2005).

44 Skamarock, W. C. et al. *A Description of the Advanced Research WRF Version 4*. NCAR Technical Note NCAR/TN-556+STR (NCAR, Boulder, CO, 2019).
45 Callewaert, S. *WRF-GHG User Guide* (Royal Belgian Institute for Space Aeronomy, 2024). https://doi.org/10.18758/Q6RAPNEU
46 Beck, V. et al. *The WRF Greenhouse Gas Model (WRF-GHG)*. Technical Report No. 25 (Max Planck Institute for Biogeochemistry, Jena, 2011).
47 Zhao, X. et al. Understanding greenhouse gas (GHG) column concentrations in Munich using the Weather Research and Forecasting (WRF) model. *Atmos. Chem. Phys.* **23,** 14325–14347 (2023).
48 Hersbach, H. et al. ERA5 hourly data on single levels from 1940 to present. Copernicus Climate Change Service (C3S) Climate Data Store (CDS) https://doi.org/10.24381/cds.adbb2d47 (2018).
49 Hersbach, H. et al. ERA5 hourly data on pressure levels from 1940 to present. Copernicus Climate Change Service (C3S) Climate Data Store (CDS) https://doi.org/10.24381/cds.bd0915c6 (2018).
50 Zhao, X. et al. Analysis of total column CO_2 and CH_4 measurements in Berlin with WRF-GHG. *Atmos. Chem. Phys.* **19,** 11279–11302 (2019).
51 Pillai, D. et al. High-resolution simulations of atmospheric CO_2 over complex terrain – representing the Ochsenkopf mountain tall tower. *Atmos. Chem. Phys.* **11,** 7445–7464 (2011).
52 Ho, D. et al. Recommended coupling to global meteorological fields for long-term tracer simulations with WRF-GHG. *Geosci. Model Dev.* **17,** 7401–7422 (2024).
53 Tilmes, S., Emmons, L. K., Buchholz, R. R. & The CESM2 Development Team. CESM2.2/CAM-chem output for boundary conditions. UCAR/NCAR Atmospheric Chemistry Observations and Modeling Laboratory https://doi.org/10.5065/XS0R-QE86 (2022).
54 Bloom, A. A. et al. CMS: global 0.5-deg wetland methane emissions and uncertainty (WetCHARTs v1.3.3). ORNL DAAC https://doi.org/10.3334/ORNLDAAC/2346 (2024).
55 Wiedinmyer, C. et al. The Fire Inventory from NCAR version 2.5: an updated global fire emissions model for climate and chemistry applications. *Geosci. Model Dev.* **16,** 3873–3891 (2023).
56 Zhou, M., Wang, P., Kumps, N., Hermans, C. & Nan, W. TCCON data from Xianghe, China, Release GGG2020.R0. CaltechDATA https://doi.org/10.14291/tccon.ggg2020.xianghe01.R0 (2022).
57 Liu, C., Wang, W., Sun, Y. & Shan, C. TCCON data from Hefei (PRC), Release GGG2020.R1. CaltechDATA https://doi.org/10.14291/tccon.ggg2020.hefei01.R1 (2023).
58 China Meteorological Administration. Mt. Waliguan (WLG) surface in situ CH_4 daily data, version 2024-06-14-0938. WMO/GAW World Data Centre for Greenhouse Gases, https://doi.org/10.50849/WDCGG_CH4_ALL_2024 (2024).
59 Holben, B. N. et al. AERONET—A federated instrument network and data archive for aerosol characterization. *Remote Sens. Environ.* **66,** 1–16 (1998).
60 Jarvis, A., Reuter, H. I., Nelson, A. & Guevara, E. Hole-filled SRTM for the globe version 4. CGIAR-CSI SRTM 90m Database https://srtm.csi.cgiar.org/ (2008).
61 Lorente, A. et al. Methane retrieved from TROPOMI: improvement of the data product and validation of the first 2 years of measurements. *Atmos. Meas. Tech.* **14,** 665–684 (2021).
62 Copernicus Sentinel-5P (processed by ESA). TROPOMI Level 2 Methane Total Column products, Version 02. European Space Agency https://doi.org/10.5270/S5P-3lcdqiv (2021).
63 Alvera-Azcárate, A., Barth, A., Sirjacobs, D. & Beckers, J.-M. Enhancing temporal correlations in EOF expansions for the reconstruction of missing data using DINEOF. *Ocean Sci.* **5,** 475–485 (2009).

64 North, G. R., Bell, T. L., Cahalan, R. F. & Moeng, F. J. Sampling errors in the estimation of empirical orthogonal functions. *Mon. Weather Rev.* **110,** 699–706 (1982).
65 Parrish, D. F. & Derber, J. C. The National Meteorological Center's spectral statistical-interpolation analysis system. *Mon. Weather Rev.* **120,** 1747–1763 (1992).
66 Li, Z. et al. A three-dimensional variational data assimilation system for multiple aerosol species with WRF/Chem and an application to $PM_{2.5}$ prediction. *Atmos. Chem. Phys.* **13,** 4265–4278 (2013).
67 Lu, F. et al. Surface-observation-constrained high-frequency coal mine methane emissions in Shanxi, China, reveal more emissions than inventories, consistent with satellite inversion. *Atmos. Chem. Phys.* **25,** 5837–5856 (2025).

Acknowledgements

This research has been funded in the framework of UNEP's International Methane Emissions Observatory (IMEO). We acknowledge Minqiang Zhou, Pucai Wang, Nicolas Kumps, Christian Hermans and Weidong Nan for the Xianghe TCCON GGG2020.R0 data, and Cheng Liu, Wei Wang, Youwen Sun and Changgong Shan for the Hefei TCCON GGG2020.R1 data. We also acknowledge the NASA AERONET program and the Xianghe site investigators for establishing and maintaining the aerosol observations used in this study. We acknowledge the China Meteorological Administration for providing the Mt. Waliguan surface in situ CH_4 observations and the WMO/GAW World Data Centre for Greenhouse Gases for distributing the data.

Author contributions

Yanqiu Liu, Jason Blake Cohen and Kai Qin developed the research question and designed the experimental program. Y.L. performed the WRF-GHG simulations and all data analysis, and drafted the manuscript. J.B.C. and K.Q. supervised the study and revised the manuscript, with J.B.C. additionally contributing to the scientific interpretation of the results and designing the impartial method to interpret WRF-GHG and TROPOMI spatially and temporally at high resolution. W.H. contributed the satellite-constrained Shanxi coal-mine emission inventory and its optimization and processing. G.H., L.S. and H.W. provided technical support for data acquisition, processing and modelling and advised on the interpretation of results. K.T. and R.A.F. contributed the UNEP-IMEO and Global Methane Pledge policy framing, proposed and emphasized the independent evaluation of the inventory against tower-based flux observations, and advised on the methane emission attribution within IMEO's Methane Science Studies. All authors discussed the results and contributed to the revision and finalization of the manuscript.

Competing interests

The authors declare no competing interests.

Supplementary Files

This is a list of supplementary files associated with this preprint. Click to download.

- 2SupplementOct16.docx
- 2SupplementOct16.docx